Ultrafast pore-loop dynamics in a AAA+ machine point to a Brownian-ratchet mechanism for protein translocation

Hisham Mazal[1,2], Marija Iljina[1], Inbal Riven[1] and Gilad Haran[1]

[1]Department of Chemical and Biological Physics, Weizmann Institute of Science, Rehovot 761001, Israel.

[2]Present Address: Max Planck Institute for Science of Light, Staudtstrasse 2, 90158 Erlangen, Germany.

Correspondence and requests for materials should be addressed to G.H. (email: gilad.haran@weizmann.ac.il)

Abstract

AAA+ ring-shaped machines, such as the disaggregation machines ClpB and Hsp104, mediate ATP-driven substrate translocation through their central channel by a set of pore loops. Recent structural studies have suggested a universal hand-over-hand translocation mechanism, in which pore loops are moving rigidly in tandem with their corresponding subunits. However, functional and biophysical studies are in discord with this model. Here, we directly measure the real-time dynamics of the pore loops of ClpB as they function in substrate threading, using single-molecule FRET spectroscopy. All pore loops undergo large-amplitude fluctuations on the microsecond timescale and change their conformation upon interaction with substrate proteins. Conformational dynamics of two of the pore loops strongly correlate with disaggregation activity, suggesting that they are the main contributors to substrate pulling through the central channel. Finally, the pore loops present differential dependence on ATP hydrolysis along the axial channel. This set of findings is rationalized in terms of an ultrafast Brownian-ratchet translocation mechanism, which likely acts in parallel to the much slower hand-over-hand process in ClpB and other AAA+ machines.

Introduction

AAA+ (ATPases associated with various activities) proteins form an abundant family of biological machines that harness the energy of ATP binding and hydrolysis to power cellular tasks such as protein unfolding, protein disaggregation, DNA helicase activity, DNA replication initiation, and cellular cargo transport (*1, 2*). These machines typically assemble into hexameric ring complexes that envelope a large central channel (*3*). Pore loops lining the axial channel are essential elements for machine activity (*3, 4*), and may exert force to pull substrates through the channel. The remarkable disaggregation machine ClpB and its eukaryotic analog Hsp104 consist of two nucleotide-binding domains (NBDs) per subunit. NBD1 contains two functional pore loops, PL1 and PL2, while NBD2 contains a single functional pore loop, PL3 (*5-8*) (Fig. 1). Both PL1 and PL3 harbor a conserved motif that involves a functionally important tyrosine residue, and their role in substrate pulling in a nucleotide-dependent manner has been demonstrated (*6, 7, 9-11*).

Recently, high-resolution structures of multiple AAA+ molecular machines have been solved by cryogenic electron microscopy (cryo-EM) (*3, 12-15*), showing that these proteins form hexameric spirals (Fig. 1b-d), rather than the fully-symmetric hexameric rings described earlier (*16*). Based on these recurrent features, it has been proposed that substrate-polypeptide threading through the central channel of the machines proceeds in a sequential, hand-over-hand manner, facilitated by rigid-body movement of the protomers with a step size equivalent to two amino acids (aa) per ATP hydrolysis cycle (*17, 18*). Since the ATP hydrolysis rate of these proteins is low, on the order of ~ 0.05 – 3.5 ATP molecules per second (*12, 13, 15, 19*), the translocation rate is expected to be slow. However, a recent single-molecule force spectroscopy study showed that, remarkably, translocation by ClpB is extremely fast, ~ 240 – 450 aa per second, and occurs in bursts of 14 – 28 aa (*20*). Studies on ClpX (*21*) and ClpA (*22*) also demonstrated substrate translocation with step sizes larger than 2 aa. Furthermore, it was found that these machines were active in translocation even when several of their six subunits were rendered inactive (*23, 24*). The strong disagreement between models based on structural studies and the results of real-time measurements is intriguing and hinders our understanding of the basis of substrate remodeling by these machines.

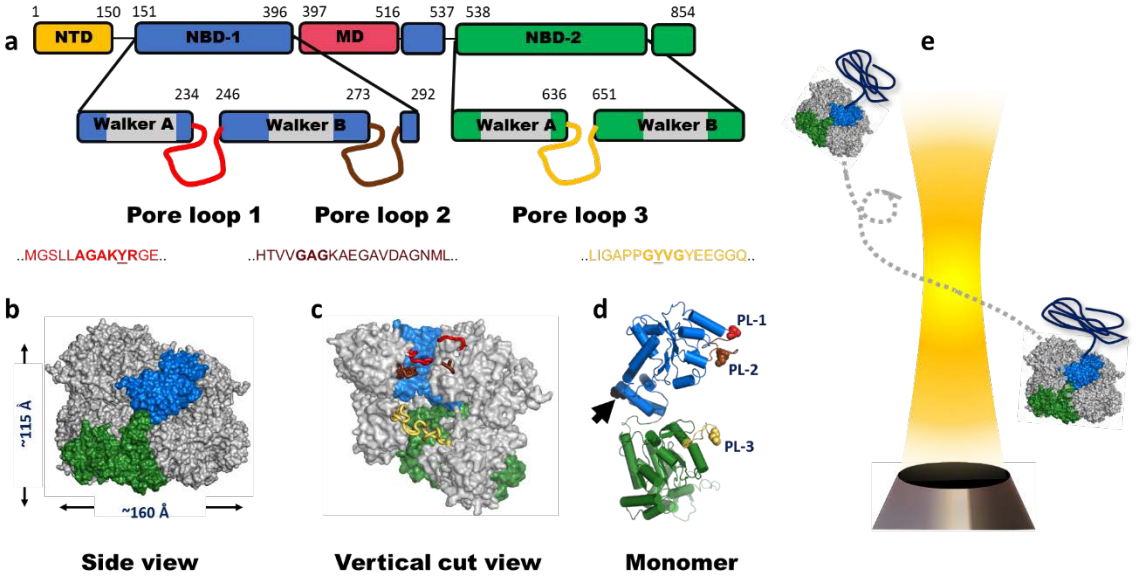

Fig. 1. ClpB domain organization and structure. (a) Domain organization of the monomer of ClpB. NTD- N-terminal domain. NBD- nucleotide binding domain. MD- middle domain. The location and sequence of pore loops are indicated on each NBD. The numbers mark residue positions in the sequence. A ClpB variant that lacks the NTD is used in this study. This variant actually occurs naturally and is fully functional. (b) Side view of the hexameric model of *E. coli* ClpB reconstructed from cryo-EM data (PDB: 6OAX). One protomer (protomer A) is highlighted using the same color code as in A. The MD and the NTD are not resolved in this structure, thus they are not shown. (c) Vertical cut view of the hexameric structure in b. PL1, PL2 and PL3 of one protomer are colored in red, brown and yellow, respectively. PL1 and PL2 are not fully resolved. (d) The monomeric structure of *E. coli* ClpB (PDB: 6OAX, protomer A), α-helices are represented as cylinders, pore loops are shown in the same color as in c. The spheres on pore loops represent the conserved tyrosine residues of PL1 (red) and PL3 (yellow), and the alanine residue of the motif GAG in PL2 (brown). Black arrow points to the position P368, which is equivalent to position S359 in *TT* ClpB, used in our smFRET experiments. (e) Freely diffusing molecules of ClpB, assembled with a single double-labeled protomer per hexamer (see Methods), emit bursts of photons as they pass through a focused laser beam, from which the FRET efficiency is calculated.

A molecular picture of the elusive pore-loop motions is critical for elucidating the translocation mechanism of such complex machines. In this work, we tackled this problem by directly observing the dynamics of pore loops in ClpB and their coupling along the axial channel, as well as their response to substrate translocation, using single-molecule FRET (smFRET) experiments (Fig. 1e) (*25*, *26*). Our hidden Markov model algorithm for photon-by-photon analysis, H^2MM (*27*), allowed us to identify microsecond motions, which we

could model in terms of two major conformational states for each pore loop. Tyrosine mutations in PL1 and PL3 exposed a correlation of the dynamics of these two pore loops with machine activity. Further, we observed differential response to ATP hydrolysis along the axial channel. These results could be rationalized in terms of a Brownian-ratchet mechanism for protein translocation by ClpB.

Results and discussion

Single-molecule studies of pore-loop dynamics

We first studied PL1, which is located on NBD1 (Fig. 1d). To probe PL1 dynamics in its complete functional form, we mutated and labeled several residues flanking its conserved motif "AGAKYR" (Fig. 1a). We found that only the variant S236C maintained disaggregation activity after labeling (Fig. 2a, Fig. S1, Table S1). We picked residue S359, located at the center of the vertical axis of the ClpB protomer, as a reference point to probe pore-loop motions along the axial channel (Fig. 1d). The same reference point was also used to study motion of the other pore loops. We thus prepared and labeled the variant S236C-S359C with donor (Alexa 488) and acceptor (Alexa 594) dyes, and assembled ClpB molecules such that only a single subunit within each ClpB hexamer was labeled. Fluorescence anisotropy measurements (Fig. S2a-d, Table S2) ruled out motional restrictions of the fluorescent dye induced by interaction with ClpB's channel or with substrate proteins (see below).

Photon-by-photon FRET trajectories were collected from labeled ClpB molecules freely diffusing through a focused laser beam in the presence of 2 mM ATP. The FRET-efficiency histogram constructed from the data (Fig. 2b, Fig. S2e) showed a major population at a FRET-efficiency value of 0.65 ± 0.01. This major peak was found to be much broader than expected based on shot noise, indicating dynamic heterogeneity (see also Fig. S2f). Donor-acceptor fluorescence cross-correlation calculated from the same data showed a rising component on a time scale of tens of microseconds, symptomatic of fast dynamics (Fig. 2c). To understand the role of PL1 in substrate engagement, we studied the effect of the

soluble model substrate κ-casein (*19*, *28*). Enhanced ATPase activity of ClpB was measured in the presence of the substrate (Fig. S1f), and its translocation was verified using the BAP-ClpP system (Fig. S1d). Importantly, in the presence of 20 μM κ-casein we noted a substrate-concentration dependent shift of the FRET-efficiency histograms toward lower values (Fig. 2b, Fig. 2d, Fig. S3a), indicating a major conformational change, though no significant substrate-induced change in the dynamics was seen in the cross-correlation function (Fig. 2c).

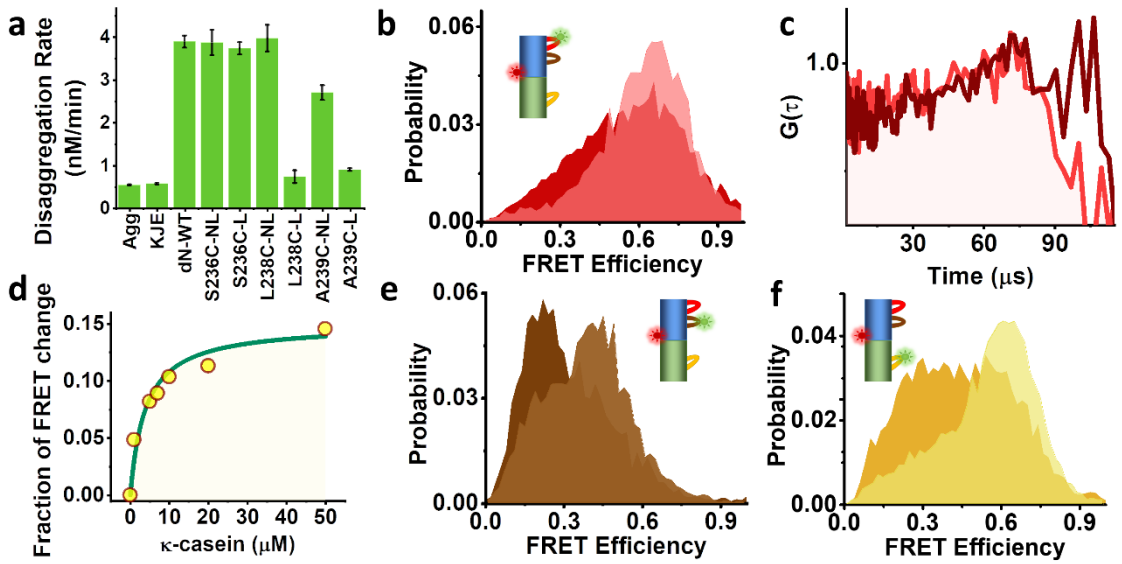

Fig. 2. Probing pore-loop conformational dynamics using smFRET: (a) Disaggregation activity of ClpB WT and PL1 mutants. Results show that all non-labeled pore loop mutants (NL) were active, but only the mutant S236C maintained activity after labeling (L). Error bars were calculated from two experiments. (b) FRET-efficiency histograms of the PL1 variant without substrate (light red), and in the presence of 20 μM κ-casein (dark red). (c) Donor-acceptor fluorescence cross-correlation functions of the PL1 variant; light red- without substrate, dark red- with substrate. (d) The relative change of the low FRET-efficiency population in histograms (Fig. S3a) as a function of κ-casein concentration. (e) FRET-efficiency histograms of the PL2 variant without substrate (light brown) and in the presence of 20 μM κ-casein (dark brown). (f) FRET-efficiency histograms of the PL3 variant without substrate (light orange) and in the presence of 20 μM κ-casein (dark orange).

To study PL2 dynamics in a similar manner (Fig. 1d, Fig. S2g,h), we mutated an alanine residue at position 281 to cysteine. The measured FRET-efficiency histogram of the

double-labeled A281C-S359C mutant was dramatically changed upon the addition of 20 μM κ-casein (Fig. 2e). The donor-acceptor fluorescence cross-correlation function again pointed to microsecond dynamics (Fig. S3b). To study PL3, we mutated Y646 close to the conserved 'GYVG' motif. The FRET-efficiency histogram of labeled S359C-Y646C in the presence of 2 mM ATP (Fig. 2f, Fig. S2i,j) changed significantly upon the addition of 20 μM κ-casein, with a substantial increase in the low FRET-efficiency shoulder. Fluorescence cross-correlation analysis showed again evidence for fast dynamics (Fig. S3c). We ruled out the involvement of NBD1-NBD2 interdomain motion in these dynamics (Fig. S3d-f).

We initially attempted to model the dynamics of each pore loop in terms of a one-dimensional free-energy surface of an arbitrary shape. To this end, we analyzed the data assuming a Markov model involving a large number of sequentially connected states (*29*). The results of this analysis are shown in Fig. 3a for PL2 and in Fig. S4a,b for PL1 and PL3, respectively. Interestingly, two well-defined potential wells, rather than a single minimum, were retrieved in each case, with microsecond time-scale jumps between them. This outcome led us to represent the data using an effective two-state model. In particular, we globally analyzed pairs of data sets measured with and without κ-casein with a two-state model (Fig. 3b and Fig. S4c-d). The results (Tables S3-S5) were validated using several methods, including stochastic recoloring of data (Fig. 3c and Fig. S5a-e), segmentation analysis to reveal the two states in FRET-efficiency histograms (Fig. 3d-e and Fig. S5f-i) and dwell-time analysis (Fig. 3f, Fig. S5j-n). In particular, dwell times obtained from the latter analysis were in good agreement with transition rates directly obtained from the H^2MM analysis of two-state model (Table S3). Using this two-state analysis, we obtained the population of each pore loop in its two states with and without substrate (Fig. S5f-i, Table S5). An effective equilibrium coefficient for the conformational dynamics of pore loop i, K_{12}^{i}, was defined as its population ratio (Table S7). Thus, for example, the population ratio in pore loop 1, K_{12}^{1} was 0.48 ± 0.01, and changed to 0.81 ± 0.01 in the presence of κ-casein (Fig. 4a). Further, we utilized the FRET-efficiency values of the two states obtained from the H^2MM analysis, together with information from ClpB structures (Table S4, Fig. S6a), to estimate the amplitude of motion of each pore loop. We calculated a motion of more than 10 Å in all cases, corresponding to as much as two substrate-protein

residues. These large fluctuations, which could not be inferred from recent static high-resolution structures (Fig. S6b-d), are likely to contribute to substrate translocation on a much faster timescale than expected based on ATP hydrolysis rates.

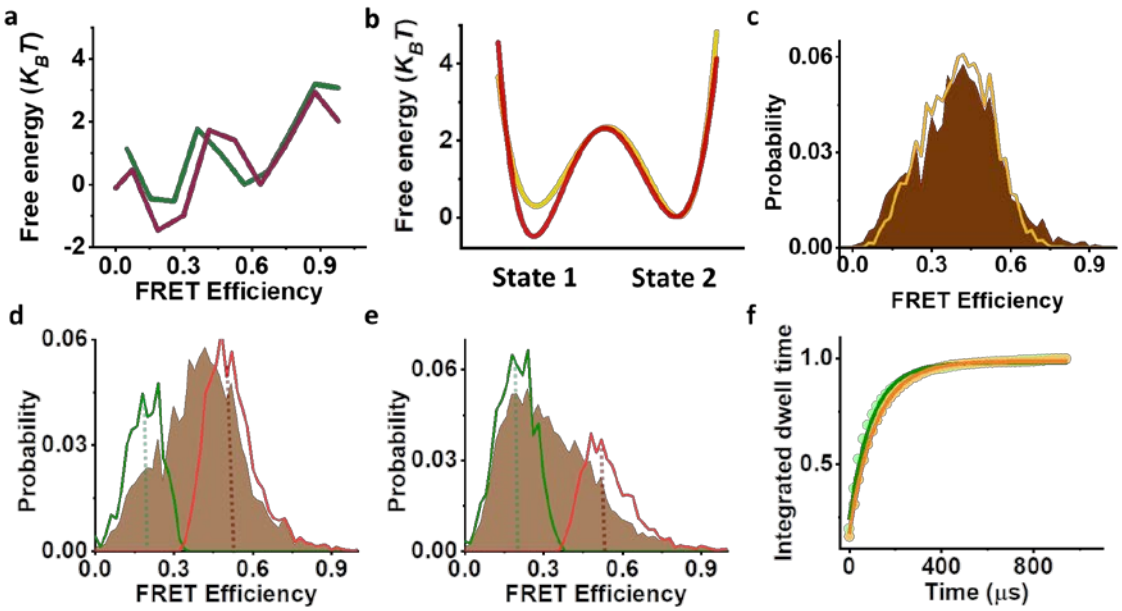

Fig. 3. Analysis of pore loop 2 conformational dynamics. (a) Free-energy profiles of PL2, as obtained from H^2MM analysis. Pore-loop FRET data in the presence of 2 mM ATP and either without (green line) or with 20 μM κ-casein (purple line), were analyzed as discussed in the Methods, using 9 sequentially-connected states. Two well-defined minima are observed, indicating a two-state system. (b) Line plots of the effective free-energy profiles as obtained from a two-state H^2MM from data measured either without (yellow line) or with 20 μM κ-casein (red line). The barrier heights in this figure were calculated using the Arrhenius equation with a pre-exponential factor of 10^5 s^{-1}. (c) A recolored FRET-efficiency histogram of PL2 (orange), obtained from analysis with a two-state model, matches well the original histogram (brown). (d-e) Segmentation analysis. Following the two-state H^2MM analysis, segmented FRET-efficiency histograms were calculated according to the procedure outlined in Methods section in order to obtain the distributions of the separate states. In each histogram, the green line is the low FRET-efficiency segmented population, and the red line is the high FRET-efficiency segmented population. Original histograms are plotted in brown. Dashed lines point to FRET-efficiency values of the two states obtained from the analysis. (d) with ATP only and (e) with ATP and 20 μM κ-casein. (f) Dwell time analysis. Integrated dwell-time distributions were calculated based on the results of the two-state H^2MM analysis as described in Methods section.

Nucleotides differentially affect pore-loop dynamics

To understand the mechanochemical coupling between ATP hydrolysis and pore-loop motions, we studied the effect of different nucleotides on the dynamics, including (in addition to ATP) ADP to mimic the post-hydrolysis state and the slowly hydrolysable analog ATPγS. Parameters derived from H^2MM analysis of measured smFRET data are

given in Tables S5, S7 and S9. To quantify the effect of nucleotides on pore-loop conformational dynamics, we computed K_{12}^{i} values from these parameters and then calculated the substrate-response factors, which are ratios of K_{12}^{i} values with and without the substrate, $R_i = K_{12}^{i}(+substrate)/K_{12}^{i}(-substrate)$ (Table S11). Surprisingly, FRET-efficiency distributions of PL1 registered in the presence of ADP, and ATPγS, were almost identical to the equivalent histograms measured with ATP, either with or without κ-casein (Fig. S7a,d). Correspondingly, K_{12}^{1} values (Fig. 4a) were very similar irrespective of the nucleotide used, and so were R_1 values (Table S11): 1.68 ± 0.01 with ATP, and similar values with ADP and ATPγS. In contrast, PL2 demonstrated a differential response to nucleotides (histograms in Fig. S7b,e, K_{12}^{2} in Fig. 4b). Accordingly, R_2 changed from 2.25 ± 0.03 in ATP to 1.67 ± 0.02 in ADP, indicating a weaker response to the substrate. Remarkably, ATPγS did not elicit any substrate-induced change in the FRET-efficiency histogram of PL2, and R_2 for this nucleotide was 1.00 ± 0.02.

In the case of PL3, the FRET-efficiency histograms (Fig. S7c,f) and K_{12}^{3} values (Fig. 4c) also showed the largest response to substrate addition in the presence of ATP, with a corresponding R_3 value of 2.28 ± 0.01, though significant changes were also registered in the presence of ADP (R_3 = 1.71 ± 0.02), and weaker response with ATPγS (R_3 = 1.34 ± 0.02).

Taken together, these results indicate that ATP hydrolysis and likely the presence of the product P_i are important for a significant shift of the free energy surfaces of PL2 and PL3 by the substrate, while PL1 is completely nucleotide-type independent.

Correlation of dynamics to disaggregation activity

To probe the correlation of pore-loop conformational changes with machine activity, we investigated mutants of the conserved tyrosine residues located on PL1 and PL3. Several studies showed that mutation of these tyrosine residues to alanines resulted in reduced machine activity, with a more pronounced effect in the case of PL3 (*6, 11, 30*). We generated either a tyrosine mutant of PL1, Y243A (Y1), a tyrosine mutant of PL3, Y643A (Y3), or a double-mutant, Y243A-Y643A (Y1-Y3). G6PDH disaggregation activity was

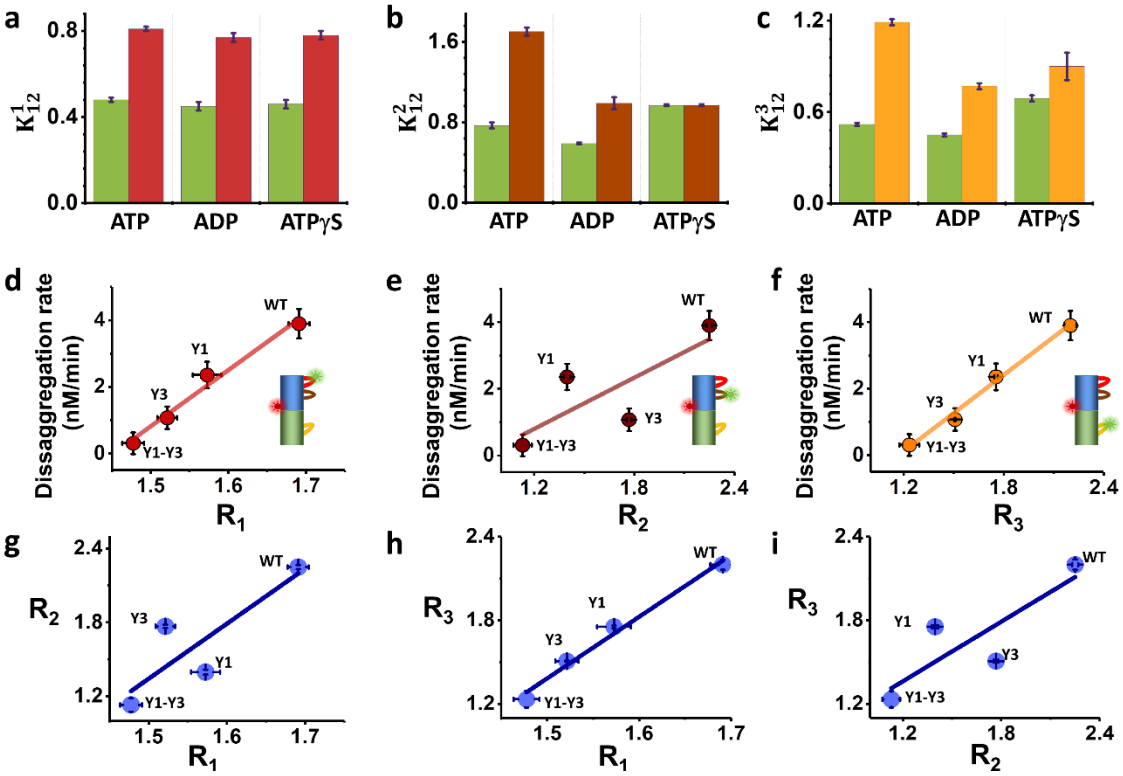

Fig. 4. Modulating pore loop conformational changes by nucleotides and tyrosine mutations. (a-c) Equilibrium coefficients for the conformational dynamics without or with 20 μM κ-casein and in the presence of different nucleotides (Table S7). (a) PL1: green- no substrate, red- with substrate. (b) PL2: green- no substrate, brown- with substrate. (c) PL3- green- no substrate, yellow- with substrate. (d-f) Correlation of disaggregation rate and the substrate-response factors, R_i, of the three pore loops in tyrosine mutants (Table S11). (g-i) Correlations between substrate-response factors of the three pore loops in tyrosine mutants. Errors were calculated from at least two experiments.

reduced in all tyrosine mutants (Fig. S1g, Table S12) (*11*, *30*), with Y3 showing a stronger activity reduction than Y1, and Y1-Y3 showing almost no disaggregation activity. smFRET measurements were performed on each pore loop in constructs bearing Y1, Y3 or Y1-Y3, in the presence of 2 mM ATP and with or without 20 μM κ-casein (Fig. S7g-o) Parameters derived from H^2MM analysis of these data are given in Tables S6, S8 and S10. Correlation analysis of the disaggregation activity of each tyrosine mutant with substrate-response factors, R_i (Fig. 4d-f, see Table S11 for the values of these parameters), demonstrated significant correlation for PL1 and PL3, with R^2 values of 0.98 and 0.95, respectively. In contrast, PL2 demonstrated a weaker correlation, with an R^2 value of 0.64. These results indicate that the conformational changes occurring in both PL1 and PL3 contribute significantly to machine activity in terms of protein translocation. The high correlation between PL3 dynamics and the overall disaggregation activity of the machine

is in line with previous findings that NBD2 is the main contributor to machine activity (*19, 31*), but the high correlation of PL1 dynamics to disaggregation is less anticipated. Strikingly, correlation plots between substrate-response factors of the different pore loops (Fig. 4g-i) demonstrated a strong correlation between PL1 and PL3, with an R^2 value of 0.99. All correlations observed here were validated through an additional calculation that did not depend on H^2MM analysis of the data, as described in the Methods section.

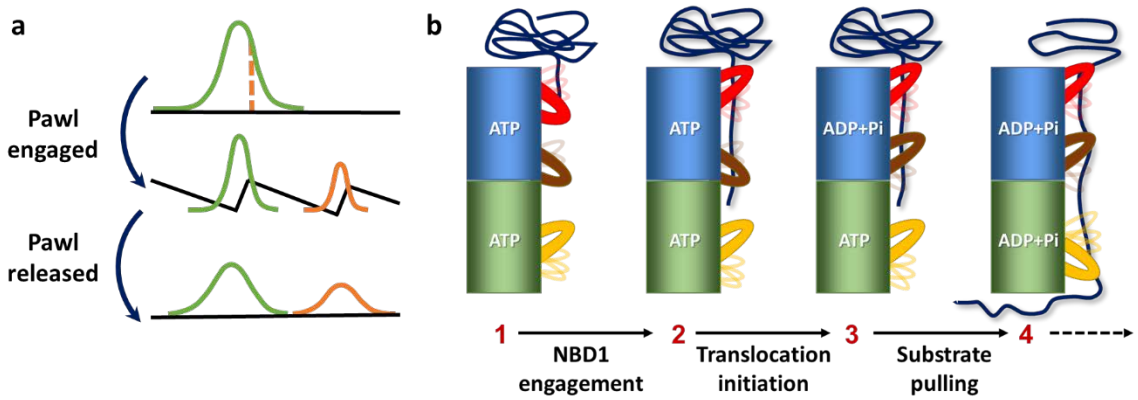

Fig. 5. Brownian-ratchet mechanism for fast substrate translocation by ClpB. (a) In a Brownian ratchet, an effective pawl periodically switches molecular dynamics between a flat free-energy surface and a structured surface, promoting unidirectional motion. (b) Model for a potential Brownian-ratchet action of pore loops. As a substrate is engaged, pore loops gradually change their average conformation even while continuing to fluctuate on the microsecond time scale between two conformational states. The change in the population ratio of the two states of PL2 and PL3, which likely takes place only upon hydrolysis of ATP, is equivalent to a shift between two free-energy surfaces, as in panel a, and turns them into effective pawls. At the same time, PL1 and PL3 function in pulling the substrate through the central channel.

Brownian-ratchet model for protein translocation by ClpB

Our findings confer a more active role to pore-loop dynamics in machine activity than perceived before. Indeed, the microsecond conformational dynamics of PL1 and PL3 are not only correlated with each other, but also strongly correlate with the disaggregation rate of the machine, and therefore also with substrate translocation rate. At the same time, both PL2 and PL3, but not PL1, seem to require nucleotide hydrolysis to change their conformation in response to substrate translocation, even though their dynamics are much

faster than ATP hydrolysis. In particular, our results suggest that the relative propensities of the two fast-exchanging states of PL2 and PL3 are modulated when substrate is added and ATP hydrolysis has occurred. In fact, our observations on PL2 are in line with a recent structural study of Hsp104 (*6).*

These remarkable results point to a Brownian-ratchet like mechanism (*32-34*) for fast substrate translocation by ClpB. In a typical Brownian-ratchet model (Fig. 5a), the input of chemical energy (e.g. ATP hydrolysis) transfers the machine between a state that allows free diffusion and a state with a pawl-like free-energy surface that rectifies the overall motion. The strong correlation between the structural changes of PL1 and PL3 and the disaggregation rate implies that these pore loops are active in pulling the substrate across ClpB's channel (Fig. 5b). At the same time, the requirement for ATP hydrolysis for PL2 and PL3 conformational changes points to these pore loops as the ratchet pawls that operate to rectify substrate motion at different stages of translocation through the channel. PL2 may act first as a pawl when the substrate interacts with NBD1 and ATP has been hydrolyzed (Fig. 5b, step 3). This result is supported by a recent optical tweezers study of ClpA, which showed that ATP hydrolysis in NBD1 is important to prevent back-slipping of a client substrate (*22*). Similar events at NBD2 may then engage PL3 as a pawl (Fig. 5b, step 4). It is possible that disengagement of these pawls allows looped polypeptide segments to escape after partial threading (*20, 35*). The protein harnesses the power of asynchronous pulling by neighboring subunits to generate rapid processive translocation events. The fast fluctuations of the pore loops allow them to reconfigure along a protein substrate, facilitating proper gripping and pulling and likely preventing premature stalling. This Brownian-ratchet mechanism is an appealing model for the operation of ClpB, even though the structural component(s) responsible for asymmetric substrate translocation remain to be identified. The Brownian ratchet can operate in parallel to the much slower hand-over-hand process. Since pore loops are highly conserved in almost all AAA+ proteins *(3, 36, 37)*, and since deviations from the predictions of the hand-over-hand mechanism have also been observed in several of them (*20-22*), it is likely that the Brownian ratchet mechanism is a general mode of operation for these machines.

Methods

Protein purification

The DNA of the *Thermus thermophilus* ClpB variant with a cleaved N-terminal domain, starting at residue 141 (ΔN-ClpB), mutants of this construct, the full length ClpB variant modified to bind ClpP protease (BAP), and the co-chaperones DnaK, DnaJ and GrpE were cloned into a pET28b vector with the addition of a six-histidine tag preceded by a tobacco etch virus protease (TEV) cleavage site, and purified exactly following our recently published protocol (*31*). ClpP was cloned in a pET9a vector with a C-terminal histidine tag and was also purified following the same purification procedure as mentioned below. Briefly, *E. coli* BL21 (DE3) pLysS cells transformed with protein vectors were grown to OD 0.9-1.0 at 37°C. Expression was induced by adding 1 mM IPTG and the cells were then incubated at 25°C overnight. Bacteria were then harvested, and the proteins were purified on a Ni-NTA resin (GE Healthcare) and dialyzed overnight in the presence of 1 mM ATP. Finally, proteins were further purified using a HiPrep DEAE FF (GE Healthcare) column equilibrated with 50 mM HEPES, 20 mM KCl and 2 mM TCEP at pH 7.4 (DEAE buffer). The peak containing the purified protein was collected, and purity was assessed by gel electrophoresis (see Fig. S1 for native gels, Table S1 for sequence with marked mutation positions and for complete list of the primers used in this study).

Protein labeling

We took advantage of the physiologically relevant ClpB version with a truncated N-terminal domain (ΔN-ClpB, from here ClpB) (*38-40*), which allowed us to directly label the pore loops without any hindrance from this domain. ClpB labeling was carried out as described in our previous work (*31*). Double-cysteine mutants were exchanged into the labeling buffer 1 (25 mM HEPES, 25 mM KCl, pH 7.1) and then reacted with the acceptor dye molecules, Alexa 594 C5 maleimide at a 1:1.2 protein to dye ratio for 2 h. Protein molecules were then separated from the unreacted dye using a desalting column (Sephadex G25, GE Healthcare), equilibrated with the same labeling buffer but including 2 M guanidinium chloride (GdmCl) to expose the partially buried sites for labeling. ClpB in 2 M GdmCl was then reacted with the donor dye Alexa 488 C5 maleimide at a 1:0.8 protein to dye ratio for 2 h. Unreacted dye molecules were then separated using a desalting column equilibrated with the labeling buffer including 2 M GdmCl. To obtain ClpB hexamers with

a single labeled protomer or less, we reassembled ClpB molecules by mixing labeled subunits with 100-fold molar excess of cysteine-less subunits according to the mixing procedure described below.

It is important to mention that in the case of the variant S236C-S359C, both sites are well exposed and might be labeled with donor and acceptor. On the other hand, in the case of A281C-S359C and S359C-Y646C, there is semi-specific labeling. In these mutants, S359C is labeled with acceptor dye and the sites A281C and Y646C are labeled with the donor.

Subunit mixing

To ensure that we indeed obtain homogeneous mixing of the labeled and the unlabeled ClpB subunits, we mixed them in a 6 M GdmCl solution, which contained 50 mM HEPES and 150 mM NaCl (the mixing buffer). Subsequently, the denaturant concentration was reduced step-by-step using dialysis, as follows: after the initial 4 h in 6 M GdmCl, the buffer was exchanged and the sample was incubated until full equilibration was reached in the mixing buffers containing 4 M GdmCl, then 2 M GdmCl, 1 M GdmCl, and, finally, 0 M GdmCl. At each step we confirmed that our samples reached equilibrium with the dialysis buffer using refractometry of the solution. Finally, the mixed subunits were further extensively dialyzed against the smFRET buffer (25 mM HEPES, 25 mM KCl, 10 mM $MgCl_2$ and 2 mM ATP, pH 7.8), to ensure their full refolding and reassembly. The 1:100 ratio of labeled to non-labeled ClpB molecules was verified by comparing the absorbance of Alexa 488 at 490 nm and the protein at 280 nm. While in general we mixed double-labeled subunits with ΔN-ClpB (WT) subunits, in the case of ClpB molecules that contained a functional mutation (Y243A, Y643A, Y243A-Y643A), the double-labeled subunits were mixed with cysteine-less variants of the same mutants. Native-gel electrophoresis, gel-filtration chromatography, enzymatic activity assays and inter-subunit FRET measurements showed that the mixed labeled ClpB molecules were assembled and active (Fig. S1). The assembled molecules were then filtered through 100 nm filters (Whatman Anotop-10), aliquoted and stored at -80°C.

ATPase activity

ATPase activity of ClpB was measured using a coupled colorimetric assay (*31*). 1 µM ClpB (desalted to 25 mM HEPES, 25 mM KCl, pH 7.8) was incubated in the presence of various amounts of ATP (50 µM – 3 mM) in 25 mM HEPES (pH 7.8), 25 mM KCl, 0.01%

TWEEN 20 and an ATP regeneration system (2.5 mM phosphoenol pyruvate, 10 unit/ml pyruvate kinase, 15 unit/ml lactate dehydrogenase, 2 mM 1,4-dithioerythritol, 2 mM EDTA, 0.25 mM NADH) at 25°C. The reaction was started by adding $MgCl_2$ to a final concentration of 10 mM. ATP hydrolysis rate was then measured indirectly by monitoring NADH absorption at 340 nm over time using micro-plate reader (Synergy HTX, BioTek). ATP hydrolysis rate at each ATP concentration was determined from the initial slope of the reaction and was background-corrected. ATP hydrolysis rate was then plotted as a function of ATP concentration and fitted to the Hill equation:

$$v = V_{max} \frac{S^n}{S^n + K_{0.5}^n}$$

where v is the initial reaction velocity, V_{max} is the maximum reaction velocity at saturating substrate concentration, S is the substrate concentration, $K_{0.5}$ is the concentration at which half of the molecules are bound and n is the Hill constant. To test the stimulation of ATP hydrolysis of ClpB, we incubated ClpB with κ-casein at target concentrations (0 – 50 μM), using the same reaction buffer as above. ATP hydrolysis rate was calculated as described above (Fig. S1e-f, Table S12)

Protein disaggregation activity

This assay was carried out as described previously (*31*). Briefly, 90 μM G6PDH from *Leuconostoc mesenteroides* was denatured by heating at 47°C for 5 min in a buffer containing 50 mM HEPES, 5 M urea, 20 mM DTT and 7.5% glycerol. Aggregate formation was achieved by diluting (1:100) the denatured G6PDH into a reactivation buffer (50 mM HEPES, 30 mM KCl, 1 mM EDTA, 1 mM TCEP, 3 mM ATP, 20 μg/μl pyruvate kinase, 3 mM phosphoenol pyruvate and 20 mM $MgCl_2$) followed by heating at 47°C for 10 min. 750 nM G6PDH aggregates were mixed with 2 μM ClpB, 4 μM DnaK, 1 μM DnaJ and 1 μM GrpE in the same reactivation buffer as before, and this disaggregation reaction mixture was incubated at 37°C. The recovered activity of G6PDH protein was then measured at different time points during the incubation, from which the rate of disaggregation was calculated, exactly as described before (*31*) (Fig. S1g, Table S12).

Protein degradation activity

To verify that ClpB can translocate κ-casein, we prepared a BAP variant of ClpB (*41*), which can bind to ClpP and transfer substrates into ClpP for degradation. The degradation

activity assay was carried out as described previously (*42*). 20 μM κ-casein was incubated with 2 μM BAP, 2.5 μM ClpP, 4 μM DnaK, 1 μM DnaJ and 1 μM GrpE, in a buffer containing 25 mM HEPES, 25 mM KCl, 10 mM $MgCl_2$ and 2 mM TCEP, pH 7.8. The reaction solution was incubated at 37°C for up to 8 h. 12 μl from each sample were withdrawn every few h during the incubation, and the reaction was quenched by mixing with Sodium dodecyl sulphate-polyacrylamide (SDS) gel sample buffer and heating at 95°C for 5 min. Finally, κ-casein concentrations were quantified by SDS gel electrophoresis. Results showed that κ-casein was degraded in the presence of BAP-ClpP system, indicating translocation of κ-casein (Fig. S1d).

Sample preparation and smFRET experiments

Samples and flow cells were prepared exactly as described in our previous publication (*31*). Single-molecule measurements were conducted on freely diffusing molecules, using a MicroTime 200 fluorescence microscope (PicoQuant). In order to sample both donor and acceptor dyes, we used pulsed interleaved excitation with 485 nm and 594 nm diode lasers pulsed at a ratio of 3:1 at a repetition rate of 40 MHz and laser power of 50 μW and 10 μW for each laser, respectively. The emitted photons were divided into two channels according to their wavelengths using a dichroic mirror (FF580-FDi01; Semrock) and filtered by band-pass filters (520/35 nm, BrightLine – Semrock, for the donor channel and ET-645/75m, Chroma, for the acceptor channel). Arrival times of these photons were registered by two single-photon avalanche photo-diodes (Excelitas SPCM-AQR-14-TR) coupled to a standalone time-correlated single photon counting module (HydraHarp 400, PicoQuant).

We detected fluorescent bursts in the single-molecule data using methods developed in the lab and described in previous studies (*31, 43, 44*). Fluorescence bursts were separated from the background photons using a cut-off time of 5 μs and only fluorescence bursts with a total of 30 photons or more were selected for further analysis. The raw FRET efficiency of each burst was then calculated based on the photons detected in both channels after donor excitation only, and the raw stoichiometry was calculated from the detected photons in both channels after both excitations. 2-D histogram of raw stoichiometry versus raw FRET efficiency was generated (Fig. S2), from which we calculated the amount of emitted donor photons leaking into the acceptor channel, and the level of direct excitation of the

acceptor dye by the 485 nm laser. We corrected the photon stream in both channels based on the calculated correction factors. To remove the donor-only and acceptor-only populations from the FRET-efficiency histograms, we selected only photon bursts with a stoichiometry that corresponded to double-labeled molecules, with both donor and acceptor dyes (Fig. S2e,g,i). Following the selection of double-labeled molecules, we selected their photons arising from donor excitation only, and analyzed these photons using burst variance analysis (*45*) (Fig. S2f,h,j), FCS and H^2MM (see below) in order to characterize and quantify the fast dynamics.

It has been suggested, based on structural models (*3*), that at each ATP hydrolysis cycle of ClpB there are 4-5 protomers engaged with the substrate and 1-2 protomers disengaged. Thus, our results are more likely (~ 83%) to represent the 4-5 engaged protomers and are less likely to represent the seam protomer (~ 17%). Furthermore, our observation time per molecule was ~ 1 ms, which is way shorter than ATP hydrolysis (Fig. S1f), so that changes in the ATP status of protomers during fluorescence burst measurements were very rare.

Per-burst fluorescence correlation spectroscopy (FCS) calculation

Cross-correlation functions of the donor and acceptor fluorescence on a burst-by-burst basis were calculated similarly to previously published methods (*46*). For the calculation, only the double-labeled species were selected (Fig. S2). An increase in the cross correlation at early times indicated fast conformational dynamics (Fig. 2c, Fig. S3b,c), while no increase indicates no detectable dynamics (Fig. S3f).

Fluorescence anisotropy measurements

Time-resolved fluorescence anisotropy experiments (Fig. S2a-d) were conducted on target proteins using the MicroTime200 fluorescence microscope (PicoQuant). Samples were diluted to 1-2 nM in the working buffer (25 mM HEPES, 25 mM KCl, 10 mM $MgCl_2$, 2 mM ATP, with and without 20 μM κ-casein) containing 0.01% TWEEN 20 and then loaded into a flow cell pre-coated with a lipid bilayer (*31*). Molecules were excited with a 485 nm diode laser pulsed at a repetition rate of 40 MHz with a power of 50 μW. Emitted photons were passed through a 50 μm pinhole and divided based on their polarization using a polarizing beam splitter cube, followed by filtration using band-pass filters (520/35 nm, BrightLine). Photon arrival times relative to the excitation pulse were registered using two

single-photon avalanche photo-diode detectors (Excelitas SPCM-AQR-14-TR) coupled to a time-correlated single-photon counting module (HydraHarp 400, PicoQuant). The parallel and perpendicular fluorescence decays were constructed from the data and background corrected. Fluorescence anisotropy decays were then calculated using the following relation: $r(t) = \frac{I_{\parallel(t)} - GI_{\perp(t)}}{I_{\parallel(t)} + 2GI_{\perp(t)}}$, where $I_{\parallel(t)}$ and $I_{\perp(t)}$ are the time-dependent fluorescence intensities of the parallel and perpendicular components, and G is the polarization sensitivity factor (whose value was determined to be 1).

Steady-state fluorescence anisotropy values were measured using a Horiba Jobin-Yvon Fluorolog fluorimeter, and these values are provided in Table S2. Steady state fluorescence anisotropy values were also calculated from the time-resolved data using the formula $r = \frac{\sum I_{\parallel(t)} - \mathrm{G} \sum I_{\perp(t)}}{\sum I_{\parallel(t)} + 2\mathrm{G} \sum I_{\perp(t)}}$ and are also listed in Table S2.

While the steady-state anisotropy values of pore-loop labels are relatively high, an observation of the anisotropy decay curves suggests that these values reflect the overall slow tumbling of the ClpB hexamer, while at short times a fast anisotropy decay uniformly appears in the data. Importantly, no significant changes in either anisotropy decay curves or steady-state values were registered upon addition of substrate proteins, indicating the absence of motional restriction by the substrate.

Comparison of single-molecule derived and cryo-EM-predicted FRET distributions

To compare our FRET data to cryo-EM derived data, we calculated a list of distances between the residues labeled in this work in pore loops of all available ClpB structures. In particular, we used PDB files 6OG1, 6OAX, 6OAY, 6RN2, 6RN3, 6RN4, 6QS6, 6QS7, SQS8, 5OG1 and 5OF1, in order to map all possible distances of these pore loops, irrespective of the conditions used. We then calculated the expected FRET-efficiency values for these distances, using a measured value for the Förster distance (54 Å) (*31*). Results are shown in Fig. S6.

H^2MM analysis

The algorithm H^2MM for photon-by-photon smFRET data analysis was introduced in Ref. (*27*). The Matlab code for H^2MM can be found at https://pubs.acs.org/doi/abs/10.1021/acs.jpcb.6b10726. The inputs for the analysis are the

arrival times of the donor and acceptor photons, which constitute the observation sequence (O). A hidden Markov chain is specified by the following components:

1) Prior matrix (Pi) (Π), Π=[π_1,π_2….π_n], which is a stochastic matrix and defines the probability of a Markov chain to start with state x out of n states.
2) A transition matrix, $A = \begin{pmatrix} a_{11} & \dots & a_{1n} \\ \dots & \dots & \dots \\ a_{n1} & \dots & a_{nn} \end{pmatrix}$,

which is also a stochastic matrix that includes all the probabilities to move between pairs of states (from x to y) out of the n available ones.

3) The observation matrix, $B = \begin{pmatrix} b_{11} & \dots & b_{1m} \\ \dots & \dots & \dots \\ a_{n1} & \dots & a_{nm} \end{pmatrix}$,

where m defines the number of observables and n defines the number of states. For simple two-color FRET experiments on the photon-by-photon level, there are only two observables, the donor and acceptor photons (m=2).

The algorithm run proceeds according to the following steps:

a) Initialization: Guess initial model parameter A, B, Π. (Here, we use 50-100 initial guesses).
b) Expectation: Given an observation sequence O and the set of states in the HMM, we learn the HMM parameters Π, A and B. This step is done iteratively using the forward-backward algorithm (Baum-Welch algorithm), a special case of the Expectation-Maximization algorithm (EM).
c) Maximization: Re-estimate Π, A and B based on estimators calculated in the previous step.
d) Determine the likelihood P(O|λ); simply, what is the probability that the observations are generated by the model. If the likelihood converged, then end and output the model; otherwise repeat the cycle from b.
e) Viterbi algorithm: Using the best model λ= (Π, A, B), calculate the most probable sequence of states. Here we take the best model (highest likelihood) from all the 50-100 initial guesses, and then run the Viterbi algorithm for this model.

Generally, we choose ~10,000 selected molecules (as described above) of each data set for analysis. In case of a 'free model', we do not restrict any model parameters $\lambda = (\Pi, A, B)$. In case of global analysis of the data with and without the substrate, we let the model parameters Π and A to be optimized freely and independently, however the observation matrix is optimized from the calculation of two data sets together.

Validation of H^2MM analysis

We validated the statistical analysis using the same procedures as outlined in (*31*). To "recolor" FRET-efficiency histograms, we kept the arrival times of photons in real experimental data fixed, but erased their color identity (i.e. whether they belong to the donor or acceptor channel, green or red). We then recolored the photons using a Monte-Carlo simulation based on the model parameters obtained from H^2MM analysis. For each burst we calculated the average FRET efficiency and plotted a new histogram to compare to the original experimental histogram. In segmentation analysis, we used the most probable sequence of states in each trajectory (burst) as obtained from the H^2MM analysis together with the Viterbi algorithm. We then calculated histograms based on the assignment of each segment to either state 1 or 2. Correct modeling should lead to separation of the two states in the histogram. Dwell-time distributions were calculated based on the results of the two-state H^2MM analysis, according to the procedure described in Ref. (*44*).

Dynamics on a 1D free-energy surface modeled with H^2MM

To represent pore-loop dynamics with a single continuous free-energy profile, we used a model of 9-10 equally spaced and sequentially connected states. To this end, we restricted the H^2MM parameters as follows:

1) Observation matrix: we assumed a continuous number of states, rather than a fixed number of states. Thus, we discretized the FRET reaction coordinate with 9-10 states with FRET-efficiency values equally distributed in the range from 0.05 to 0.98.
2) Transition probability matrix: we allowed sequential transitions only, namely, all transitions a_{ij} that fulfil: i=1:N, and j=i ± [0:1]. All the rest were set to zero.
3) Prior matrix (Π): no restrictions were set on the prior matrix.

Following these restrictions, we analyzed the data with H^2MM model using 50 random initial guesses. We then took the results from the run that converged to the highest likelihood. The free-energy profile was then calculated from the occupancy of the states as follows: $V(E) = -K_B T \ln$ (probability of the state) (Fig. S4a-c).

Validation of correlation analyses (Fig. 4)

We validated the correlations shown in Fig. 4 using a method that did not depend on the H^2MM analysis and the calculation of response factors (R_i). To this end, we split each FRET-efficiency histogram into two different regions, a low FRET-efficiency region and a high FRET-efficiency region. The splitting point was determined based on the intersection point of the low and high FRET-efficiency states as obtained from segmentation analysis (Fig. S5f-i). We calculated areas below and above the splitting point and used them to obtain new values for the equilibrium constants and for the response factors. Using these values to plot correlations as in Fig. 4d-i, we obtained very similar results, with disaggregation activity strongly correlated with R_1 and R_3, and in turn a strong correlation of these two response factors.

Supplementary Information

Figs. S1-S7.

Tables S1-S12.

References

1. P. I. Hanson, S. W. Whiteheart, AAA+ proteins: have engine, will work. *Nat Rev Mol Cell Biol* **6**, 519-529 (2005).
2. T. Ogura, A. J. Wilkinson, AAA+ superfamily ATPases: common structure-diverse function. *Genes Cells* **6**, 575-597 (2001).
3. C. Puchades, C. R. Sandate, G. C. Lander, The molecular principles governing the activity and functional diversity of AAA+ proteins. *Nat Rev Mol Cell Biol* **21**, 43-58 (2020).
4. A. Martin, T. A. Baker, R. T. Sauer, Pore loops of the AAA+ ClpX machine grip substrates to drive translocation and unfolding. *Nat Struct Mol Biol* **15**, 1147-1151 (2008).
5. A. N. Rizo *et al.*, Structural basis for substrate gripping and translocation by the ClpB AAA+ disaggregase. *Nat Commun* **10**, 2393 (2019).
6. J. Lee *et al.*, Structural determinants for protein unfolding and translocation by the Hsp104 protein disaggregase. *Biosci Rep* **37**, (2017).
7. J. Hinnerwisch, W. A. Fenton, K. J. Furtak, G. W. Farr, A. L. Horwich, Loops in the central channel of ClpA chaperone mediate protein binding, unfolding, and translocation. *Cell* **121**, 1029-1041 (2005).
8. S. Lee *et al.*, The Structure of ClpB. *Cell* **115**, 229-240 (2003).
9. P. Rodriguez-Aliaga, L. Ramirez, F. Kim, C. Bustamante, A. Martin, Substrate-translocating loops regulate mechanochemical coupling and power production in AAA+ protease ClpXP. *Nature Structural & Molecular Biology* **23**, 974-981 (2016).
10. A. O. Olivares, T. A. Baker, R. T. Sauer, Mechanistic insights into bacterial AAA+ proteases and protein-remodelling machines. *Nat Rev Microbiol* **14**, 33-44 (2016).
11. S. M. Doyle, J. R. Hoskins, S. Wickner, DnaK chaperone-dependent disaggregation by caseinolytic peptidase B (ClpB) mutants reveals functional overlap in the N-terminal domain and nucleotide-binding domain-1 pore tyrosine. *J Biol Chem* **287**, 28470-28479 (2012).
12. A. H. de la Pena, E. A. Goodall, S. N. Gates, G. C. Lander, A. Martin, Substrate-engaged 26S proteasome structures reveal mechanisms for ATP-hydrolysis-driven translocation. *Science* **362**, (2018).
13. C. Puchades *et al.*, Structure of the mitochondrial inner membrane AAA+ protease YME1 gives insight into substrate processing. *Science* **358**, (2017).
14. C. Deville *et al.*, Structural pathway of regulated substrate transfer and threading through an Hsp100 disaggregase. *Sci Adv* **3**, e1701726 (2017).
15. S. N. Gates *et al.*, Ratchet-like polypeptide translocation mechanism of the AAA+ disaggregase Hsp104. *Science* **357**, 273-279 (2017).
16. S. Lee, B. Sielaff, J. Lee, F. T. Tsai, CryoEM structure of Hsp104 and its mechanistic implication for protein disaggregation. *Proc Natl Acad Sci U S A* **107**, 8135-8140 (2010).
17. S. E. Glynn, J. R. Kardon, O. Mueller-Cajar, C. Cho, AAA+ proteins: converging mechanisms, diverging functions. *Nat Struct Mol Biol* **27**, 515-518 (2020).
18. J. Shorter, D. R. Southworth, Spiraling in Control: Structures and Mechanisms of the Hsp104 Disaggregase. *Cold Spring Harb Perspect Biol* **11**, (2019).
19. C. Deville, K. Franke, A. Mogk, B. Bukau, H. R. Saibil, Two-Step Activation Mechanism of the ClpB Disaggregase for Sequential Substrate Threading by the Main ATPase Motor. *Cell Rep* **27**, 3433-3446 e3434 (2019).
20. M. J. Avellaneda *et al.*, Processive extrusion of polypeptide loops by a Hsp100 disaggregase. *Nature* **578**, 317-320 (2020).
21. M. E. Aubin-Tam, A. O. Olivares, R. T. Sauer, T. A. Baker, M. J. Lang, Single-molecule protein unfolding and translocation by an ATP-fueled proteolytic machine. *Cell* **145**, 257-267 (2011).

22. H. C. Kotamarthi, R. T. Sauer, T. A. Baker, The Non-dominant AAA+ Ring in the ClpAP Protease Functions as an Anti-stalling Motor to Accelerate Protein Unfolding and Translocation. *Cell Reports* **30**, 2644-2654.e2643 (2020).
23. O. Iosefson, A. O. Olivares, T. A. Baker, R. T. Sauer, Dissection of Axial-Pore Loop Function during Unfolding and Translocation by a AAA+ Proteolytic Machine. *Cell Rep* **12**, 1032-1041 (2015).
24. K. L. Zuromski, R. T. Sauer, T. A. Baker, Modular and coordinated activity of AAA+ active sites in the double-ring ClpA unfoldase of the ClpAP protease. *Proc Natl Acad Sci U S A* **117**, 25455-25463 (2020).
25. H. Mazal, G. Haran, Single-molecule FRET methods to study the dynamics of proteins at work. *Current Opinion in Biomedical Engineering* **12**, 8-17 (2019).
26. E. Lerner *et al.*, Toward dynamic structural biology: Two decades of single-molecule Förster resonance energy transfer. *Science* **359**, eaan1133 (2018).
27. M. Pirchi *et al.*, Photon-by-Photon Hidden Markov Model Analysis for Microsecond Single-Molecule FRET Kinetics. *J Phys Chem B* **120**, 13065-13075 (2016).
28. K. M. Woo, K. I. Kim, A. L. Goldberg, D. B. Ha, C. H. Chung, The heat-shock protein ClpB in Escherichia coli is a protein-activated ATPase. *Journal of Biological Chemistry* **267**, 20429-20434 (1992).
29. R. Ramanathan, V. Munoz, A Method for Extracting the Free Energy Surface and Conformational Dynamics of Fast-Folding Proteins from Single Molecule Photon Trajectories. *J Phys Chem B* **119**, 7944-7956 (2015).
30. Y. Nakazaki, Y. H. Watanabe, ClpB chaperone passively threads soluble denatured proteins through its central pore. *Genes Cells* **19**, 891-900 (2014).
31. H. Mazal *et al.*, Tunable microsecond dynamics of an allosteric switch regulate the activity of a AAA+ disaggregation machine. *Nature Communications* **10**, 1438 (2019).
32. W. Hwang, M. Karplus, Structural basis for power stroke vs. Brownian ratchet mechanisms of motor proteins. *Proc Natl Acad Sci U S A* **116**, 19777-19785 (2019).
33. J. Howard, Protein power strokes. *Curr Biol* **16**, R517-519 (2006).
34. R. D. Astumian, S. Mukherjee, A. Warshel, The Physics and Physical Chemistry of Molecular Machines. *Chemphyschem* **17**, 1719-1741 (2016).
35. T. Haslberger *et al.*, Protein disaggregation by the AAA+ chaperone ClpB involves partial threading of looped polypeptide segments. *Nat Struct Mol Biol* **15**, 641-650 (2008).
36. S. M. Siddiqui, R. T. Sauer, T. A. Baker, Role of the processing pore of the ClpX AAA+ ATPase in the recognition and engagement of specific protein substrates. *Genes Dev* **18**, 369-374 (2004).
37. S. R. White, B. Lauring, AAA+ ATPases: achieving diversity of function with conserved machinery. *Traffic* **8**, 1657-1667 (2007).
38. C. L. Squires, S. Pedersen, B. M. Ross, C. Squires, ClpB is the Escherichia coli heat shock protein F84.1. *Journal of Bacteriology* **173**, 4254-4262 (1991).
39. A. K. Clarke, M. J. Eriksson, The truncated form of the bacterial heat shock protein ClpB/HSP100 contributes to development of thermotolerance in the cyanobacterium Synechococcus sp strain PCC 7942. *J Bacteriol* **182**, 7092-7096 (2000).
40. M. Iljina, H. Mazal, P. Goloubinoff, I. Riven, G. Haran, Entropic Inhibition: How the Activity of a AAA+ Machine Is Modulated by Its Substrate-Binding Domain. *ACS Chem Biol* **16**, 775-785 (2021).
41. J. Weibezahn *et al.*, Thermotolerance requires refolding of aggregated proteins by substrate translocation through the central pore of ClpB. *Cell* **119**, 653-665 (2004).
42. R. Rosenzweig, S. Moradi, A. Zarrine-Afsar, J. R. Glover, L. E. Kay, Unraveling the mechanism of protein disaggregation through a ClpB-DnaK interaction. *Science* **339**, 1080-1083 (2013).

43. E. Sherman, G. Haran, Coil-globule transition in the denatured state of a small protein. *Proc Natl Acad Sci U S A* **103**, 11539-11543 (2006).
44. H. Y. Aviram *et al.*, Direct observation of ultrafast large-scale dynamics of an enzyme under turnover conditions. *Proc Natl Acad Sci U S A* **115**, 3243-3248 (2018).
45. J. P. Torella, S. J. Holden, Y. Santoso, J. Hohlbein, A. N. Kapanidis, Identifying molecular dynamics in single-molecule FRET experiments with burst variance analysis. *Biophys J* **100**, 1568-1577 (2011).
46. M. Wahl, I. Gregor, M. Patting, J. Enderlein, Fast calculation of fluorescence correlation data with asynchronous time-correlated single-photon counting. *Opt. Express* **11**, 3583-3591 (2003).

Acknowledgements

We thank Dr. Rina Rosenzweig for the generous gift of the BAP-ClpP plasmids and for helpful discussions. We further thank Drs. Hagen Hofmann and Pierre Goloubinoff for their careful reading of the manuscript. We also thank Demian Libermann for his help in some of the calculations. H.M. was supported by Planning & Budgeting Committee of the Council of Higher Education of Israel. M.I. is the recipient of an EMBO Long-Term Fellowship (ALTF 317–2018) and the IASH Fellowship for International Postdoctoral Fellows. G.H. is funded by the European Research Council (ERC) under the European Union's Horizon 2020 research and innovation programme (grant agreement No 742637). G.H. is the incumbent of the Hilda Pomeraniec Memorial Professorial Chair.

Author contributions: H.M. and G.H. conceived the project. H.M and and M.I. performed the experiments with help from I.R. All authors wrote the manuscript.

Competing interests: the authors declare no competing interests.

Data and materials availability: All data needed to evaluate the conclusions in the paper are present in the paper and/or the Supplementary Materials.

Supplementary Information

Ultrafast pore-loop dynamics in a AAA+ machine point to a Brownian-ratchet mechanism for protein translocation

Hisham Mazal[1,2], Marija Iljina[1], Inbal Riven[1] and Gilad Haran[1]

[1]Department of Chemical and Biological Physics, Weizmann Institute of Science, Rehovot 761001, Israel.

[2]Present Address: Max Planck Institute for Science of Light, Staudtstrasse 2, 90158 Erlangen, Germany.

Correspondence and requests for materials should be addressed to G.H. (email:gilad.haran@weizmann.ac.il)

This PDF file includes:

Figs. S1-S7.
Tables S1-S12.

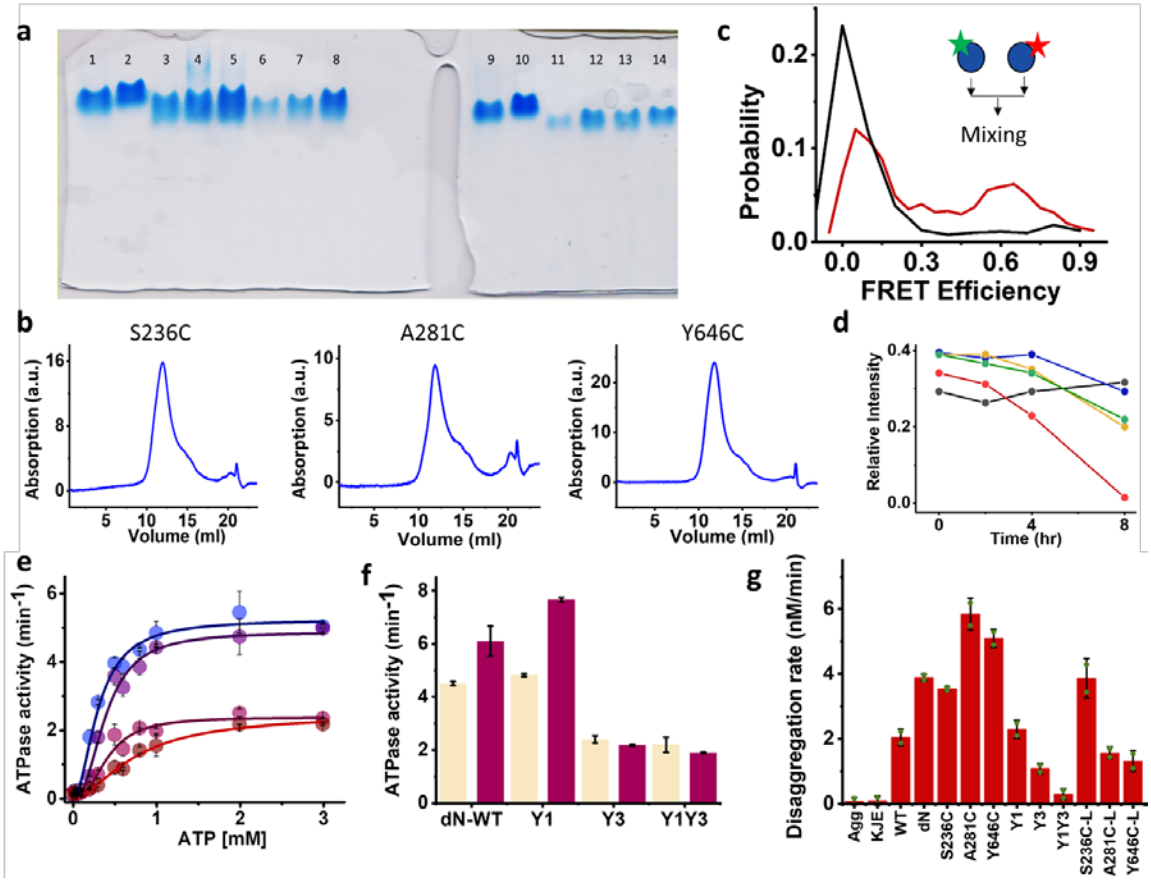

Fig. S1. Characterization of ΔN-ClpB mutants. (a) Native gel electrophoresis (3 % acrylamide), run in the presence of 10 mM $MgCl_2$ and 2 mM ATP. (1) Full length (FL) WT *TT* ClpB, (2) FL WT *TT* ClpB S428C–S771C, double-labeled with Alexa 488 and Alexa 594, and mixed 1:100 with cysteine-less FL ClpB. (3) Double-labeled ΔN-ClpB A281C-S359C mixed 1:100 with WT ΔN-ClpB. (4-5) Repeats of double-labeled ΔN-ClpB S359C-Y646C mixed 1:100 with WT ΔN-ClpB. (6) Double-labeled ΔN-ClpB S359C-Y646C-Y243A mixed 1:100 with ΔN-ClpB Y243A mutant. (7) Double-labeled ΔN-ClpB S359C-Y646C-Y643A mixed 1:100 with ΔN-ClpB Y643A mutant. (8) Double-labeled ΔN-ClpB S359C-Y646C-Y243A-Y643A mixed 1:100 with ΔN-ClpB Y243A-Y643A mutant. (9) FL WT *TT* ClpB, same as (1). (10) Same as 2. (11) Double-labeled ΔN-ClpB S236C-359C mixed 1:100 with WT ΔN-ClpB. (12) Double-labeled ΔN-ClpB S236C-S359C-Y243A mixed 1:100 with ΔN-ClpB Y243A mutant. (13) Double-labeled ΔN-ClpB S236C-S359C-Y643A mixed 1:100 with ΔN-ClpB Y643A mutant. (14) Double-labeled ΔN-ClpB S236C-S359C-Y243A-Y643A mixed 1:100 with ΔN-ClpB Y243A-Y643A mutant. The gel was stained with Coomassie Blue (a). We only observed one band in each case, indicating homogeneity of the samples. (b) Size-exclusion chromatography of labeled and assembled constructs. ΔN-ClpB single cysteine mutants PL1 (S236C), PL2 (A281C) and PL3 (Y646C) were purified and fully labeled with Alexa 594. The proteins were run on a SEC column (Superdex 200, 10/300 GL, total volume 23.6 ml) to qualitatively determine their assembly. ClpB molecules were diluted in 25 mM HEPES, 25 mM KCl, 10 mM $MgCl_2$ and 2 mM ATP. The labeled ClpB molecules eluted within the narrow peak at ~ 12 ml, confirming their assembly. As a reminder, in our single-molecule experiments, we mixed the labeled molecules in 1:100 ratio with non-labeled ClpB to obtain hexamers with only a single labeled protomer. Thus, ClpB hexamers should be assembled even better as there would be

no steric clashes between labeled protomers. (c) Validation of ClpB integrity under the smFRET experimental conditions. This experiment was done similarly to the previously published protocol (*31*). Here, ClpB single cysteine mutant (S236C) was purified, assembled and labeled with either Alexa 488 (donor) or Alexa 594 (acceptor), separately. We then mixed the donor and acceptor variants of each labeled mutant at a 1:1 ratio, and at a final concentration of 5 nM (inset). The mixing process was done using 6 M guanidinium chloride (GdmCl) followed by dialysis to 0 M GdmCl. We split the samples into two test tubes, one containing 2 mM ATP, and the other without ATP. We then performed smFRET experiments, to measure FRET-efficiency distribution as an indication of assembly. Black curve is S236C without ATP, which shows no high FRET-efficiency population, indicating the absence of assembly. Red curve is S236C with 2 mM ATP, showing a high FRET-efficiency population, an indication of assembly. The large peak at low FRET efficiency represents donor-only molecules. (d) Degradation of κ-casein by BAP and ClpP, performed according to the protocol in Ref. (*42*), except that the reaction was performed at 25°C rather than 55°C. The concentration of each component was as follows: 20 μM κ-casein, 2 mM ATP, 2 μM BAP and 2.5 μM ClpP, 4 μM DnaK, 1 μM DnaJ and GrpE. The reaction, containing different components, was let to proceed for 8 h. Samples at different time points were analyzed using SDS-PAGE, and the band intensity of κ-casein was measured using Image J. Black line is κ-casein alone. Blue line is κ-casein and BAP only. Green line is κ-casein and ClpP only. Orange line is κ-casein, BAP and ClpP only. Red line is κ-casein, BAP, ClpP, DnaK, DnaJ and GrpE (KJE). Red line demonstrates almost full degradation of κ-casein after 8 h. (e-g) ATPase and disaggregation activity of ΔN-ClpB pore-loop mutants. (e) ATPase activity assay was carried out according to a recently published protocol (*31*). 1 μM ΔN-ClpB was incubated in the presence of various concentrations of ATP (0 - 3 mM) at 25°C. The initial ATP hydrolysis rate was measured at each ATP concentration using a coupled enzymatic reaction (*31*). Data were then plotted and fitted to Hill equation, to extract the reaction velocity (V_{max}), the half-maximum concentration $K_{0.5}$ and the Hill coefficient n for each measurement. Dots represent the experimental data, and solid lines are the fits. Blue: ΔN-ClpB WT, dark purple: ΔN-ClpB Y243A, light purple: ΔN-ClpB Y643A, brown: ΔN-ClpB Y243A-Y643A. ΔN-ClpB WT data yielded a V_{max} value of 4.5 ± 0.5 min^{-1}, a $K_{0.5}$ value of 300 ± 20 μM and a Hill coefficient of 2.0 ± 0.3. Values for other mutants are listed in Table S12. (f) ATP hydrolysis rate of each ΔN-ClpB mutant with 2 mM ATP (light orange bars) and with 2 mM ATP and 20 μM κ-casein (purple bars) are shown for comparison. (g) G6PDH disaggregation activity assay was conducted similarly to the previously published protocol (*31*). Disaggregation rates were extracted from a time-course experiment and plotted for each ClpB mutant (see Table S12 for tyrosine mutant disaggregation activity). Agg - aggregates only. KJE - aggregates with DnaK, DnaJ and GrpE only. WT - full-length WT ClpB. dN - ΔN-ClpB. S236C, A281C and Y646C are ΔN-ClpB pore-loop single-cysteine mutants (non-labeled). Y1, Y3 and Y1-Y3 are ΔN-ClpB pore-loop tyrosine mutants, Y243A, Y643A and Y243A-Y643A, respectively. S236C-L, A281C-L and Y646C-L are ΔN-ClpB pore-loop single-cysteine mutants, labeled with Alexa 594. All ClpB proteins were incubated with aggregates and the KJE system. The error bars were calculated from two repeats of each experiment. Green dots are actual experimental measurements, while red bars are averages. Errors shown here and in all the other figures correspond to standard errors of the mean.

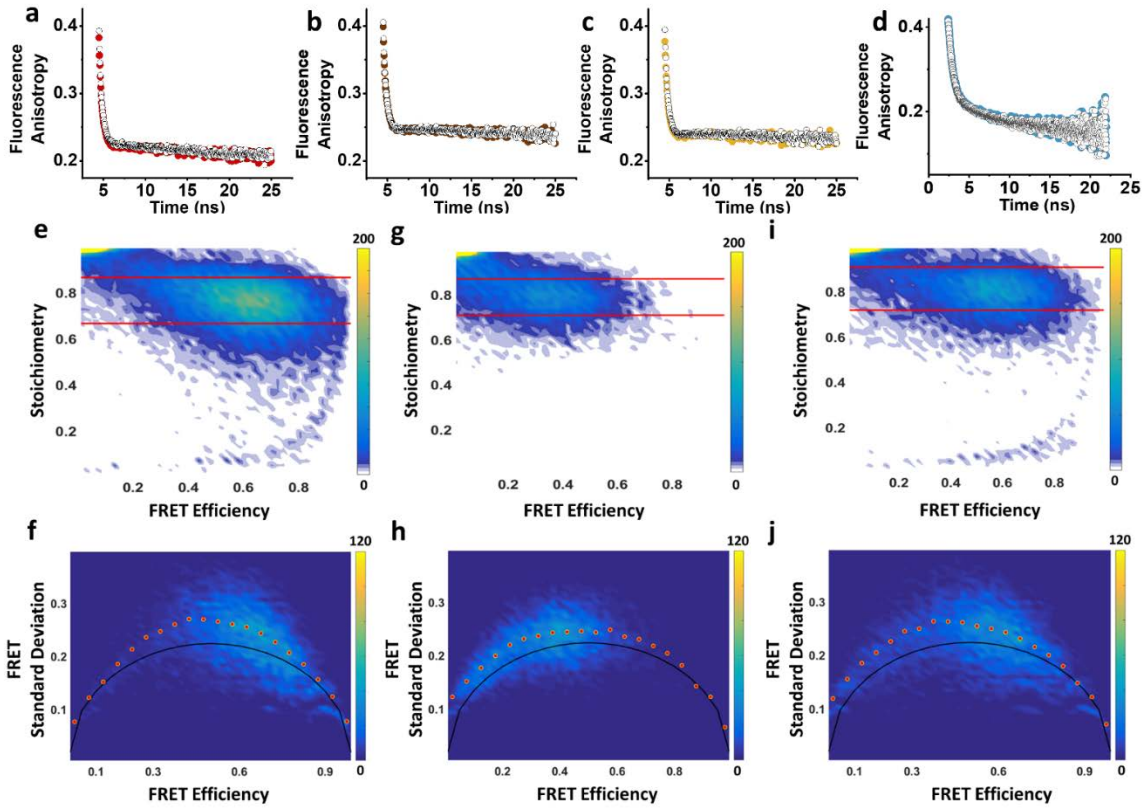

Fig. S2. Analysis of single molecules. (a-d) Time-resolved fluorescence anisotropy measurements of singly labeled pore-loops. Single cysteine variants of ΔN-ClpB were fully labeled with Alexa 488 dye, and then mixed with 1:100 ratio of cysteine-less ΔN-ClpB variant. Mixing and assembly of the complexes were done as described in the Methods section. Samples were diluted to 1-2 nM in the presence of 2 mM ATP, with and without 20 μM κ-casein, and were then measured as described in Methods. (a) ΔN-ClpB S236C with and without κ-casein, shown as black and red dots, respectively. (b) ΔN-ClpB A281C, with (black) and without (brown) κ-casein. (c) ΔN-ClpB Y646C with (black) and without (yellow) κ-casein. (d) ΔN-ClpB S359C with (black) and without (blue) κ-casein. Importantly, no difference in any of the fluorescence anisotropy decays was observed upon the addition of κ-casein. (e-j) 2D FRET-Stoichiometry histograms and burst variance analysis (BVA) plots of ClpB molecules. smFRET experiments with different double-labeled ΔN-ClpB mutants were conducted in the presence of 2 mM ATP. From each experimental data set, a 2D histogram of stoichiometry vs. FRET efficiency was created from ~10,000 burst events as described in the Methods section. The double-labeled species is found at a stoichiometry of 0.6-0.8, the donor-only species at a stoichiometry above 0.96 and the acceptor-only species at a stoichiometry below 0.3. Only bursts of the double-labeled species (marked with red lines) were taken for further analysis (e, g and i). BVA was performed for these selected double-labeled species (*45*) (f, h and j). Black line represents the expected theoretical standard deviation based on shot noise, whereas the blue cloud is the burst-by-burst standard deviation, and the red dots show averaged standard deviation values in bins of size 0.05. The experimental standard deviation values are above the theoretical line, an indication of dynamic heterogeneity. (e, f) ΔN-ClpB (S236C-S359C). (g, h) ΔN-ClpB (A281C-S359C). (i, j) ΔN-ClpB (S359C-Y646C).

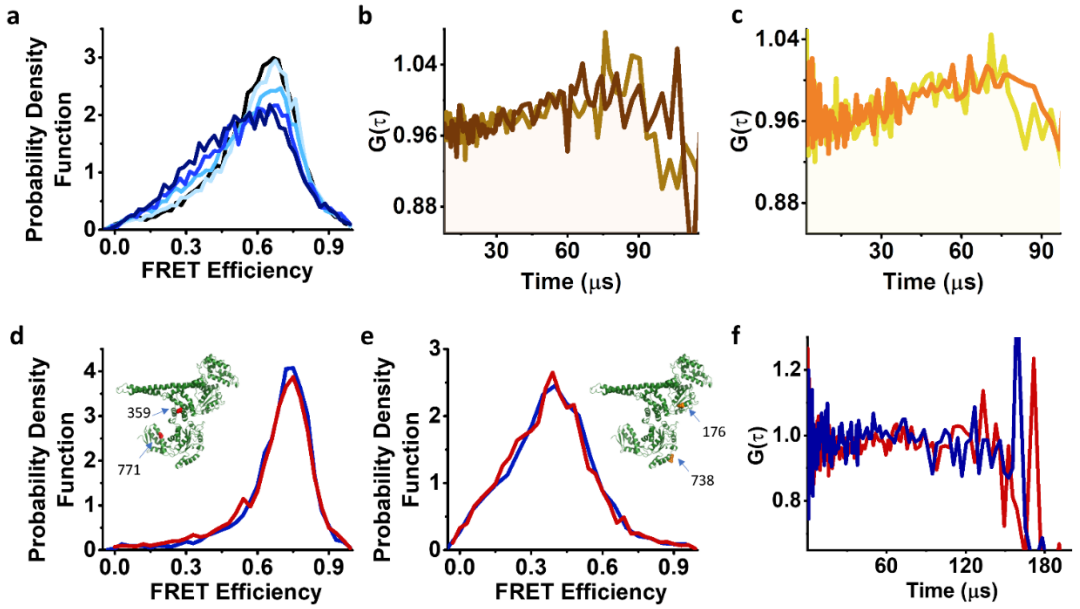

Fig. S3. Additional single-molecule measurements. (a) κ-casein binding to PL1 measured by smFRET. ΔN-ClpB S236C-S359C was incubated with increasing concentrations of κ-casein (0-50 μM), and FRET efficiency histograms were recorded. FRET histograms become broader with increasing κ-casein concentrations. Light blue to dark blue lines represents the data at 1, 5, 20 and 50 μM κ-casein, respectively. This data set was used to construct the curve in Fig. 2d of the main text. (b-c) Fast dynamics in PL2 and PL3 but not between the NBDs. Donor-acceptor fluorescence cross-correlation functions, calculated from the smFRET measurements of (b) A281C-S359C; light brown- without substrate, dark brown- with substrate and (c) S359C-Y646C; light orange- without substrate, dark orange- with substrate. Both results indicate fast dynamics, on the order of tens of microseconds, with and without substrate. (d-f) NBD1-NBD2 FRET efficiency histograms. (d) ΔN-ClpB was labeled at positions S359C and S771C with Alexa 488 and Alexa 594 fluorescent dyes, and then mixed in 1:100 ratio with the cysteine-less variant. The FRET-efficiency histogram in the presence of 2 mM ATP is shown in blue, and the FRET efficiency histogram in the presence of 2 mM ATP and 20 μM κ-casein is shown in red. (e) Another probe of NBD1-NBD2 dynamics, using the pair D176C-Q738C. Color code is the same as in (d). From both panels, we can conclude that there is no effect of κ-casein on NBD1-NBD2 conformational dynamics. (f) Donor-acceptor cross-correlation curves of the construct D176C-Q783C, with (red) and without (blue) κ-casein, do not detect any NBD1-NBD2 interdomain dynamics on the microsecond time scale.

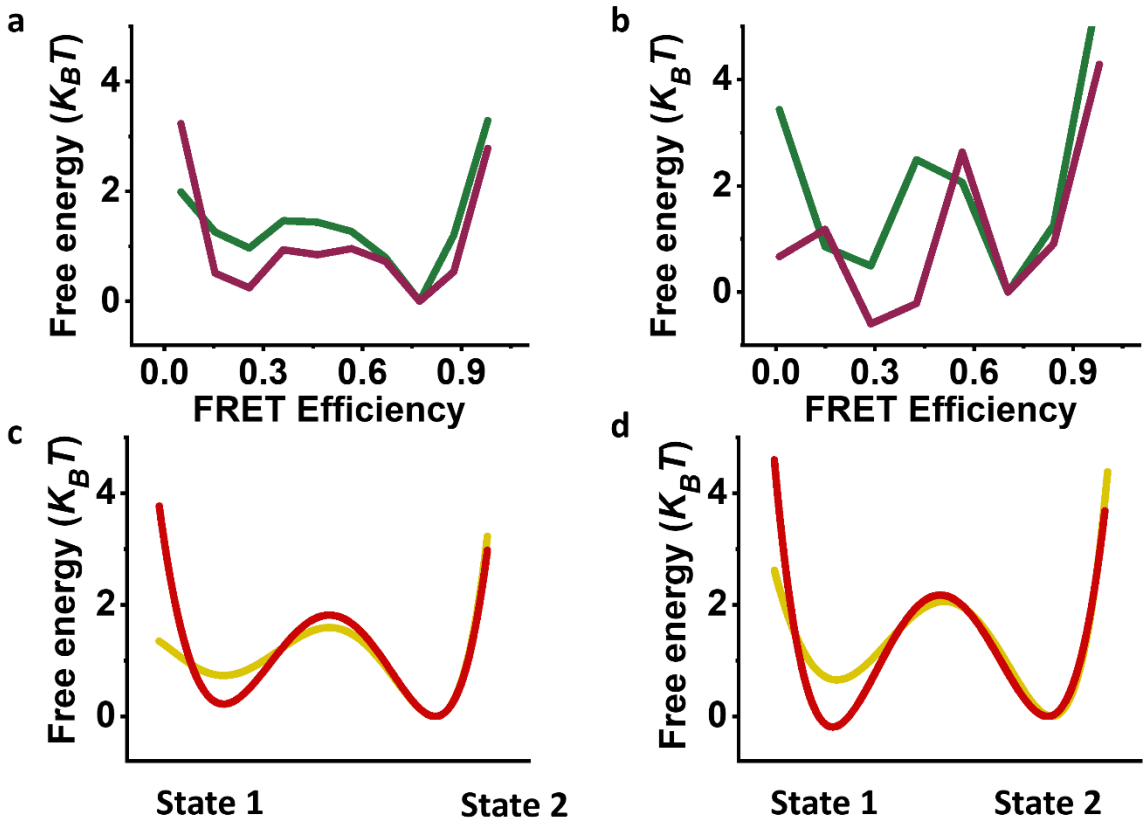

Fig. S4. Energy landscape as obtained from H²MM analysis. (a-b) Line plots of the free-energy profiles of pore loops, as obtained from H²MM analysis. Pore-loop FRET data measured in the presence of 2 mM ATP and either without (green line) or with 20 μM κ-casein (purple line), were analyzed as discussed in Methods, using 9 sequentially connected states. The free-energy profile was calculated from state propensities. (a) PL1 (ΔN-ClpB S236C-S359C). (b) PL3 (ΔN-ClpB S359C-Y646C). The analysis suggests that a two-state model is appropriate to describe the data, as in the case of PL2 (Fig. 3 of the main text). (c-d) Line plots of the effective free-energy profiles as obtained from H²MM analysis using a two-state model, in the presence of 2 mM ATP and either without (yellow line) or with 20 μM κ-casein (red line). The free-energy profiles were calculated using H²MM parameters as indicated in Tables S3-S5. The barrier heights were calculated using the Arrhenius equation with a pre-exponential factor of 10^5 s^{-1}. (c) PL1 (ΔN-ClpB S236C-S359C) and (d) PL3 (ΔN-ClpB S359C-Y646C).

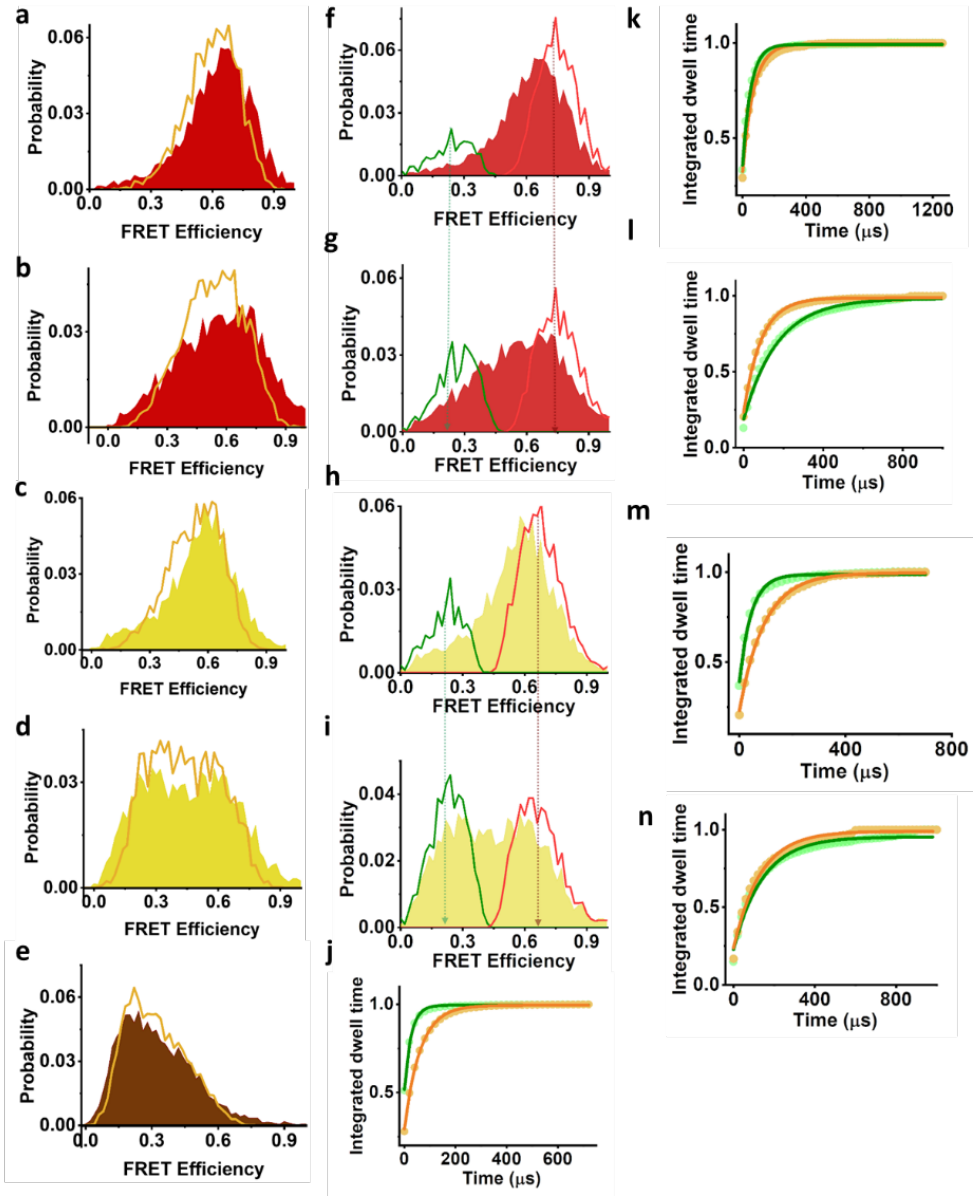

Fig. S5. H²MM data analysis. (a-e) Recoloring of FRET-efficiency histograms. FRET-efficiency histograms were recolored based on the results of H²MM analysis with a two-state model, following the procedure outlined in the Methods section of the main text and Ref. (*31*). Recolored histograms are shown as orange lines. (a-b) ΔN-ClpB S236C-S359C, without and with 20 μM κ-casein, respectively. (c-d) ΔN-ClpB S359C-Y646C, without and with 20 μM κ-casein, respectively. (e) ΔN-ClpB A281C-S359C, with 20 μM κ-casein. (f-i) Segmentation analysis. Following the two-state H²MM analysis, FRET-efficiency histograms were segmented according to the procedure outlined in the Methods section and Ref. (*31*) in order to obtain the distributions of the separate states. In each histogram, green line is the low FRET population, and red line is the high FRET population, as obtained from the segmentation analysis. Arrows point to FRET-efficiency values of the two states obtained from the analysis. (f-g) ΔN-ClpB S236C-S359C, without and with 20 μM κ-casein, respectively. (h-i) ΔN-ClpB S359C-Y646C, without and with 20 μM κ-casein, respectively. In all pore-loop data, an increase in low FRET population was observed in the

presence of 20 μM κ-casein. H^2MM model parameters are listed in Tables S3-S5. (j-n) Dwell time analysis. Integrated dwell-time distributions were calculated based on the results of the two-state H^2MM analysis, according to the procedure described in Ref. (*44*). State 1 is shown as green dots, and state 2 is shown as orange dots. Green and orange solid lines are fits to single-exponential functions, and the obtained rates are listed in Table S3. (j-k) S236C-S359C without and with 20 μM κ-casein, respectively. (l) A281C-S359C with 20 μM κ-casein. (m-n) S359C-Y646C without and with 20 μM κ-casein, respectively.

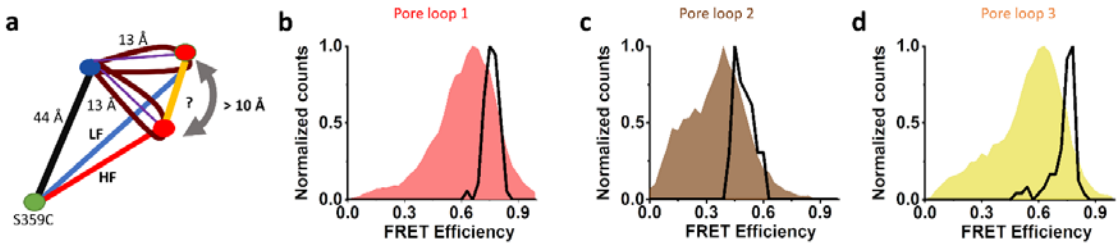

Fig. S6. Pore-loop conformational space as obtained from smFRET experiments and predicted from cryo-EM data. (a) Triangulation calculation to obtain the approximate movements of PL1 (thick purple curves) vertically along the axial channel (orange line), around their pivot point (blue dot). Purple lines represent the approximate distance between the labeled position on PL1 and the pivot point, assumed to be fixed at 13 Å. Black line represents the distance to S359C, which is also assumed to be fixed at 44 Å. Blue and red lines are the extracted distances of the experimental high FRET-efficiency and low FRET-efficiency states, respectively. With the given distances, we calculated a distance of more than 10 Å (~ 2 amino acids), as the possible amplitude of pore-loop motion along the axial channel (vertically). This result, and similar calculations for PL2 and PL3, indicate that measured pore-loop dynamics represent functionally significant fluctuations. The fixed distances were obtained from a cryo-EM structure of ClpB (PDB: 5og1, protomer F) (*14*). The calculation does not take into account the contribution of dye linkers to the distance changes, and may therefore slightly overestimate the amplitude of motion. (b-d) Pore-loop distances (S236C, A281C, Y646C) were measured relative to our reference point (S359C), from various available cryo-EM structures of *E. coli* ClpB (*5*, *14*, *19*). Using a Förster distance of 54 Å, we converted these distances to FRET efficiencies. The resulting 'theoretical' FRET-efficiency distributions are plotted as black lines, together with the experimental FRET-efficiency distributions (area plots) for each pore loop, for comparison. (b) S236C-S359C. (c) A281C-S359C. (d) S359C-Y646C. The experimental smFRET histograms are much broader than obtained from cryo-EM structures, indicating that the pore loops sample a much larger conformational space than can be gleaned from frozen structures.

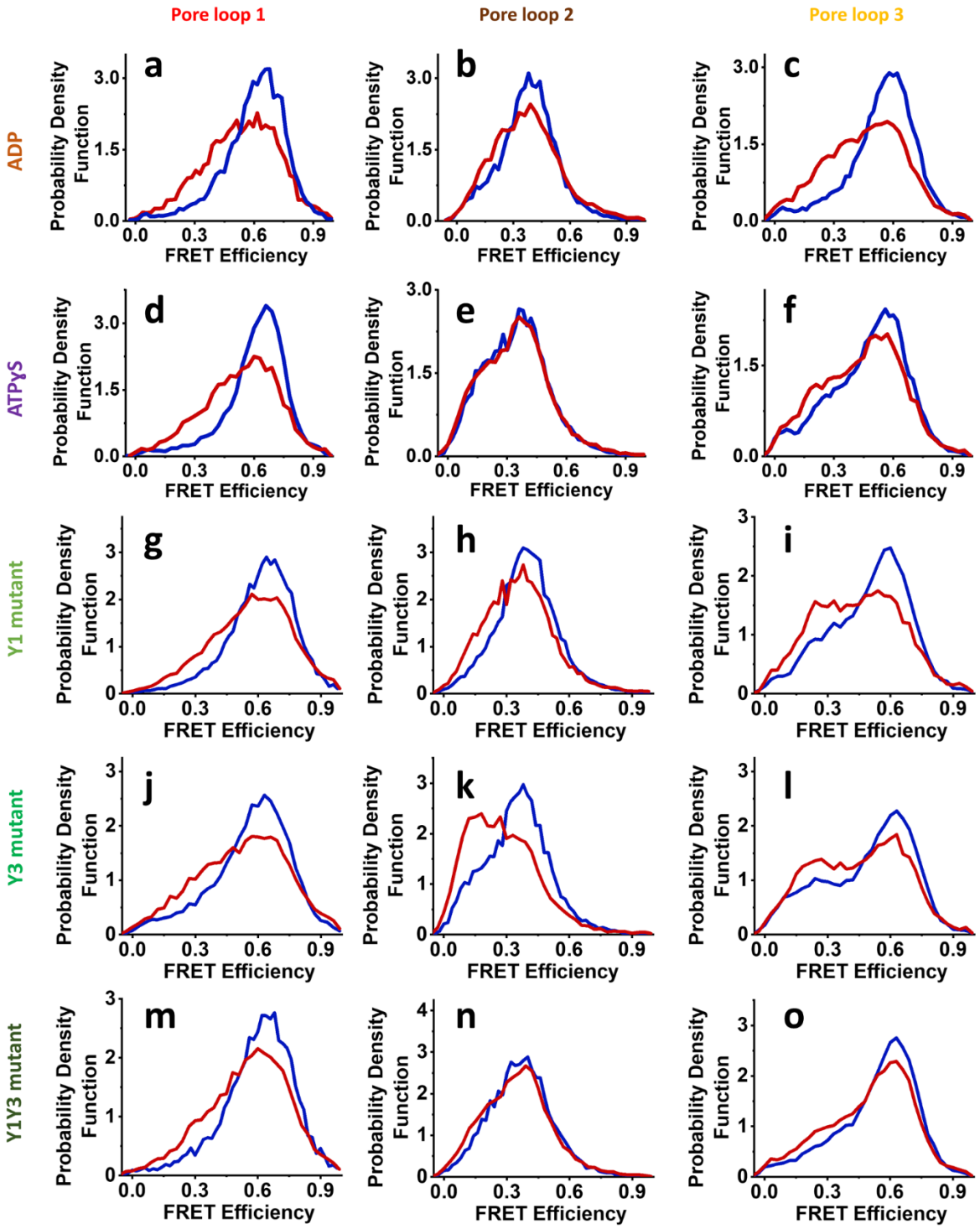

Fig. S7. The effects of different nucleotides and tyrosine mutations on the induction of conformational changes of pore loops by a protein substrate. FRET-efficiency histograms were measured for the three pore loops (PL1-PL3) under a series of conditions as indicated. Left column- PL1. Middle column- PL2, right column- PL3. In each panel, blue line is without substrate and red line is with 20 μM κ-casein. (a-c) 2 mM ADP. (d-f) 2 mM ATPγS. (g-i) Y1 mutant. (j-l) Y3. (m-o) Y1-Y3.

Table S1. Sequence of ClpB and list of primers for all ClpB mutants.

```
TT 1 MNLERWTQAAR-E-ALAQAQVLAQRMKH--QAIDLP-HLW-AVLLKDE-RSLAWRLLEKA 53
EC 1 MRLDRLTN--KFQLALADAQSLA--LGHDNQFIE-PLHLMSA-LLNQEGGSVS-PLLTSA 53

TT 54 G--ADPKALK-EL-QERELARLPKVE--GAEVGQYLTSR-L-SGALNRAEALMEELK-DR 104
EC 54 GINAG-Q-LRTDINQA--LNRLPQVEGTGGDV-Q--PSQDLVR-VLNLCDKLAQK-RGDN 104

TT 105 YVAVDTL-VLALA-EATPG-LPG-LEALKG---A-L-K--E-LRGGRTVQTEHAE-STYN 151
EC 105 FISSE-LFVLA-ALESR-GTLADILKA-AGATTANITQAIEQMRGGESVNDQGAEDQR-Q 159

TT 152 ALEQYGIDLT-RLAAE-GKLDPVIGRDEEIRRVIQILLRRTKNNPVLIGEPGVGKTAIVE 209
EC 160 ALKKYTIDLTER-A-EQGKLDPVIGRDEEIRRTIQVLQRRTKNNPVLIGEPGVGKTAIVE 217

TT 210 GLAQRIVKGDVPEGLKGKRIVSLQMGSLLAGAKYRGEFEERLKAVIQEVV-QSQGEVILF 268
EC 218 GLAQRIINGEVPEGLKGRRVLALDMGALVAGAKYRGEFEERLKGVLNDLAKQ-EGNVILF 276

TT 269 IDELHTVVGAGKAEGAVDAGNMLKPALARGELRLIGATTLDEYRE-IEKDPALERRFQPV 327
EC 277 IDELHTMVGAGKADGAMDAGNMLKPALARGELHCVGATTLDEYRQYIEKDAALERRFQKV 336

TT 328 YVDEPTVEETISILRGLKEKYEVHHGVRISDSAIIAAATLSHRYITERRLPDKAIDLIDE 387
EC 337 FVAEPSVEDTIAILRGLKERYELHHHVQITDPAIVAAATLSHRYIADRQLPDKAIDLIDE 396

TT 388 AAARLRMALESAPEEIDALERKKLQLEIEREALKKEKDPD-SQERLKAI-EAEIA-KLTE 444
EC 397 AASSIRMQIDSKPEELDRLDRRIIQLKLEQQALMKESD-EASKKRLDMLNE-ELSDK--E 452

TT 445 -EIAKLRAEWERER-EIL---RKLREAQHRLDEVRREIELAERQY-DLNRAAELRYGELP 498
EC 453 RQYSELEEEWKAEKAS-LSGTQTIK-AE--LEQAKIAIEQA-RRVGDLARMSELQYGKIP 507

TT 499 KLEAEVEALSEKLRG-A-RFVR-LEVTE-EDIAEIVSRWTGIPVSKLLEGEREKLLRLEE 554
EC 508 ELEKQLEAATQ-LEGKTMRLLRN-KVTDAE-IAEVLARWTGIPVSRMMESEREKLLRMEQ 564

TT 555 ELHKRVVGQDEAIRAVADAIRRARAGLKDPNRPIGSFLFLGPTGVGKTELAKTLAATLFD 614
EC 565 ELHHRVIGQNEAVDAVSNAIRRSRAGLADPNRPIGSFLFLGPTGVGKTELCKALANFMFD 624

TT 615 TEEAMIRIDMTEYMEKHAVSRLIGAPPGYVGYEEGGQLTEAVRRRPYSVILFDEIEKAHP 674
EC 625 SDEAMVRIDMSEFMEKHSVSRLVGAPPGYVGYEEGGYLTEAVRRRPYSVILLDEVEKAHP 684

TT 675 DVFNILLQILDDGRLTDSHGRTVDFRNTVIILTSNLGSPLILE--G-LQKGWPYERIRDE 731
EC 685 DVFNILLQVLDDGRLTDGQGRTVDFRNTVVIMTSNLGSDLIQERFGELD----YAHMK-E 739

TT 732 -VFKVLQQH-FRPEFLNRLDEIVVFRPLTKEQ-IRQIVEIQL-S-YLRARLAEKR-ISLE 785
EC 740 LVLGVVS-HNFRPEFINRIDEVVVFHPLG-EQHIASIAQIQLKRLY-K-RL-EERGYEIH 794

TT 786 LT-EAAKDFLAERGYDPVFGARPLRRVIQRELETPLAQKILAGE-VKEGDRV-QVDVGPA 842
EC 795 ISDEALK-LLSENGYDPVYGARPLKRAIQQQIENPLAQQILSGELVP-G-KVIRLEVNED 851

TT 843 GLVFAV-PARVEA 854
EC 852 RIV-AVQ------ 857
```

Name	Sequence
S236C	5’ gtctccttgcagatgggc**tgc**ctcctcgccggggccaag 3’
L238C	5’ ccttgcagatgggctccctc**tgc**gccggggccaagtaccgggg 3’
A239C	5’ cagatgggctccctcctc**tgc**ggggccaagtaccg 3’
Y243A (PL1 tyrosine mutant)	5’ cctcgccggggccaag**gcc**cggggcgagtttgaggagc 3’

Name	Sequence
A281C	5’ gtggtgggggcaggcaag**tgc**gagggcgccgtggacgcg 3’
S359C	5’ gtgcgcatctccgac**tgc**gccatcatcgccgcc 3’
Y643A (PL3 tyrosine mutant)	5’ cggggccccgcccggc**gcc**gtgggctacgaggagggggg 3’
Y643A (PL3 tyrosine mutant) on Y646C mutant	5’ cggggccccgcccggc**gcc**gtgggc**tgc**gaggagggggg 3’
Y646C	5’ ccccgcccggctacgtgggc**tgc**gaggagggggggcagctca 3’

The first part of this table shows sequence alignment of *TT* ClpB with *E. coli* (EC) ClpB. PL1 labeling site is marked by a red rectangle, PL2 labeling site is marked by a brown rectangle and PL3 labeling site is marked by an orange rectangle. Tyrosine mutants are marked with green rectangles. S359 is highlighted in orange. Note that in all experiments in this study, ΔN-ClpB of *TT* ClpB without the first 140 residues was used, the start of which is marked with a black box. The alignment was done using Sequence Manipulation Suite, Pairwise Align Protein Tool, and using scoring matrix BLOSUM 80. The second part includes all primers used in this work.

Table S2. Photophysical properties of fluorescent dyes attached to ClpB.

Construct	Steady-state anisotropy	Steady-state anisotropy calculated from time-resolved measurements	Quantum yield
S236C + Alexa 488 (ATP)	0.307 ± 0.004	0.278 ± 0.002	0.71 ± 0.06
S236C + Alexa 488 (ATP + κ-casein)	0.303 ± 0.007	0.276 ± 0.002	-
A281C + Alexa 488 (ATP)	0.263 ± 0.004	0.277 ± 0.002	0.72 ± 0.08
A281C + Alexa 488 (ATP + κ-casein)	0.264 ± 0.003	0.275 ± 0.002	-
Y646C + Alexa 488 (ATP)	0.235 ± 0.003	0.25 ± 0.001	0.71 ± 0.05
Y646C + Alexa 488 (ATP + κ-casein)	0.249 ± 0.004	0.25 ± 0.001	-
S359C + Alexa 488 (ATP)	0.205 ± 0.003	0.20 ± 0.02	N.D.
S359C + Alexa 488 (ATP + κ-casein)	0.203 ± 0.001	0.20 ± 0.05	-

Table S3. State-to-state transition rates (in s^{-1}) obtained from H^2MM analysis of ClpB constructs, compared to dwell times obtained as in Fig. S5.

	k_{12}		k_{21}		$k_{12}+k_{21}$	
Construct	**H^2MM**	**Dwell time**	**H^2MM**	**Dwell time**	**H^2MM**	**Dwell time**
PL1	45960 ± 5100	37660 ± 1100	22130 ± 2500	16300 ± 220	68090 ± 7600	53960 ± 1320
PL1 + κ-casein	21450 ± 1600	19300 ± 500	17500 ± 1700	14500 ± 300	38950 ± 3300	33800 ± 800
PL2	12300 ± 750	10300 ± 300	9580 ± 200	8750 ± 100	21880 ± 950	19050 ± 400
PL2 + κ-casein	6500 ± 800	5900 ± 200	11200 ± 1700	11300 ± 300	17700 ± 2500	17200 ± 500
PL3	24500 ± 100	22200 ± 950	12800 ± 100	10600 ± 200	37300 ± 200	32800 ± 1150
PL3 + κ-casein	8700 ± 1000	6400 ± 300	10400 ± 1500	7500 ± 200	19100 ± 2500	13900 ± 500

The errors were calculated from two independent repeats of the experiment.

Table S4. FRET efficiency values of pore loop states as obtained from H^2MM analysis.

Pore loop	**FRET value** State 1	**FRET value** State 2
PL1	0.240 ± 0.005	0.76 ± 0.005
PL2	0.180 ± 0.005	0.54 ± 0.005
PL3	0.210 ± 0.005	0.68 ± 0.005

Table S5. State populations of pore loops from experiments with different nucleotides and either with or without the substrate, as obtained from H^2MM analysis.

	ATP		**ADP**		**ATPγS**	
Pore loop	**State 1**	**State 2**	**State 1**	**State 2**	**State 1**	**State 2**
PL1	0.32 ±0.01	0.68 ± 0.01	0.30 ± 0.02	0.70 ± 0.02	0.30 ± 0.01	0.70 ±0.01
PL1 + κ-casein	0.45 ±0.01	0.55 ± 0.01	0.44 ± 0.02	0.56 ± 0.02	0.44 ± 0.02	0.56 ±0.02
PL2	0.43 ±0.01	0.57 ± 0.01	0.37 ± 0.02	0.63 ± 0.02	0.50 ± 0.01	0.50 ±0.01
PL2 + κ-casein	0.63 ±0.01	0.37 ± 0.01	0.51 ± 0.01	0.49 ± 0.01	0.50 ± 0.01	0.50 ±0.01
PL3	0.34 ±0.01	0.66 ± 0.01	0.31 ± 0.01	0.69 ± 0.01	0.40 ± 0.01	0.60 ±0.01
PL3 + κ-casein	0.54 ±0.01	0.46 ± 0.01	0.44 ± 0.01	0.56 ± 0.01	0.47 ± 0.01	0.53 ±0.01

The errors were calculated from two independent repeats of the experiment.

Table S6. State populations of pore loops in tyrosine mutants with and without substrate, as obtained from H^2MM analysis.

	WT		Y1		Y3		Y1-Y3	
Pore loop	**State 1**	**State 2**	**State 1**	**State 2**	**State 1**	**State 2**	**State 1**	**State 2**
PL1	0.32 ±0.01	0.68 ± 0.01	0.27 ± 0.02	0.73 ± 0.02	0.35 ± 0.01	0.65 ± 0.01	0.30 ± 0.01	0.70 ± 0.01
PL1 + κ-casein	0.45 ± 0.01	0.55 ± 0.01	0.37 ± 0.02	0.63 ± 0.02	0.45 ± 0.02	0.55 ± 0.02	0.38 ± 0.01	0.62 ± 0.01
PL2	0.43 ± 0.01	0.57 ± 0.01	0.37 ± 0.02	0.63 ± 0.02	0.46 ± 0.01	0.54 ± 0.01	0.44 ± 0.01	0.56 ± 0.01
PL2 + κ-casein	0.63 ± 0.01	0.37 ± 0.01	0.44 ± 0.01	0.56 ± 0.01	0.60 ± 0.01	0.40 ± 0.01	0.47 ± 0.01	0.53 ± 0.01
PL3	0.34 ± 0.01	0.66 ± 0.01	0.38 ± 0.01	0.62 ± 0.01	0.40 ± 0.01	0.60 ± 0.01	0.30 ± 0.01	0.70 ± 0.01
PL3 + κ-casein	0.54 ± 0.01	0.46 ± 0.01	0.52 ± 0.01	0.48 ± 0.01	0.50 ± 0.01	0.50 ± 0.01	0.37 ± 0.01	0.63 ± 0.01

The errors were calculated from two independent repeats of the experiment.

Table S7. Equilibrium constants, K_{12}^{i}, for pore-loop conformational dynamics as obtained from H^2MM analysis in the presence of different nucleotides.

	Nucleotide			Nucleotide + κ-casein		
Pore loop	**ATP**	**ADP**	**ATPγS**	**ATP**	**ADP**	**ATPγS**
PL1	0.48 ± 0.01	0.45 ± 0.02	0.46 ± 0.02	0.81 ± 0.01	0.77 ± 0.02	0.78 ± 0.02
PL2	0.76 ± 0.03	0.59 ± 0.01	0.97 ± 0.01	1.70 ± 0.04	0.99 ± 0.06	0.97 ± 0.01
PL3	0.52 ± 0.01	0.45 ± 0.01	0.69 ± 0.02	1.19 ± 0.02	0.77 ± 0.02	0.90 ± 0.09

The errors were calculated from two independent repeats of the experiment.

Table S8. Equilibrium constants, K_{12}^{i}, from experiments with tyrosine mutants as obtained from H²MM analysis.

	ATP				ATP + κ-casein			
Pore loop	**WT**	**Y1**	**Y3**	**Y1-Y3**	**WT**	**Y1**	**Y3**	**Y1-Y3**
PL1	0.48 ± 0.01	0.37 ± 0.01	0.53 ± 0.02	0.42 ± 0.01	0.81 ± 0.01	0.59 ± 0.02	0.81 ± 0.01	0.61 ± 0.01
PL2	0.76 ± 0.03	0.58 ± 0.02	0.86 ± 0.03	0.77 ± 0.02	1.70 ± 0.04	0.80 ± 0.03	1.47 ± 0.02	0.87 ± 0.03
PL3	0.52 ± 0.01	0.61 ± 0.01	0.63 ± 0.03	0.44 ± 0.02	1.12 ± 0.02	1.07 ± 0.01	0.95 ± 0.03	0.58 ± 0.02

The errors were calculated from two independent repeats of the experiment.

Table S9. State-to-state transition rates (in s^{-1}) obtained from H²MM analysis of ClpB constructs in the presence of different nucleotides.

	ATP		ADP		ATPγS	
Construct	k_{12}	k_{21}	k_{12}	k_{21}	k_{12}	k_{21}
PL1	45960 ± 5100	22130 ± 2500	44800 ± 1700	19800 ± 600	42500 ± 9000	18500 ± 600
PL1 + κ-casein	21450 ± 1600	17500 ± 1700	24000 ± 500	18000 ± 100	22500 ± 3000	17500 ± 1100
PL2	12300 ± 750	9580 ± 200	22800 ± 1100	13500 ± 300	12600 ± 300	12400 ± 200
PL2 + κ-casein	6500 ± 800	11200 ± 1700	12700 ± 1900	13500 ± 2800	11800 ± 900	11500 ± 1100
PL3	24500 ± 100	12800 ± 100	33400 ± 800	15300 ± 100	23500 ± 3000	15600 ± 2500
PL3 + κ-casein	8700 ± 1000	10400 ± 1500	18000 ± 300	14000 ± 200	15500 ± 1300	14000 ± 2500

The errors were calculated from two independent repeats of the experiment.

Table S10. State-to-state transition rates (in s^{-1}) obtained from H^2MM analysis of ClpB tyrosine mutants.

	WT		Y1		Y3		Y1-Y3	
Construct	k_{12}	k_{21}	k_{12}	k_{21}	k_{12}	k_{21}	k_{12}	k_{21}
PL1	45960 ± 5100	22130 ± 2500	48300 ± 1000	18200 ± 2500	35000 ± 1800	18700 ± 500	48800 ± 900	20000 ± 200
PL1 + κ-casein	21450 ± 1600	17500 ± 1700	29400 ± 1300	17500 ± 1700	20500 ± 300	16700 ± 500	27600 ± 300	16800 ± 200
PL2	12300 ± 750	9580 ± 200	26300 ± 300	15400 ± 100	17100 ± 200	14600 ± 500	20400 ± 300	16000 ± 100
PL2 + κ-casein	6500 ± 800	11200 ± 1700	17100 ± 200	13700 ± 200	8500 ± 300	12600 ± 500	14600 ± 200	12800 ± 100
PL3	24500 ± 100	12800 ± 100	23300 ± 800	14400 ± 600	15300 ± 300	10000 ± 100	23000 ± 500	10300 ± 100
PL3 + κ-casein	8700 ± 1000	10400 ± 1500	14200 ± 200	15300 ± 400	10900 ± 700	10500 ± 500	18100 ± 400	10500 ± 300

The errors were calculated from two independent repeats of the experiment.

Table S11. Substrate-response factors, R_i, as obtained from H^2MM analysis.

	Nucleotide			Tyrosine mutants		
Pore loop	**ATP**	**ADP**	**ATPγS**	**Y1**	**Y3**	**Y1-Y3**
PL1	1.68 ± 0.01	1.71 ± 0.02	1.69 ± 0.02	1.59 ± 0.02	1.52 ± 0.01	1.46 ± 0.01
PL2	2.25 ± 0.03	1.67 ± 0.02	1.00 ± 0.02	1.39 ± 0.02	1.76 ± 0.01	1.12 ± 0.05
PL3	2.28 ± 0.01	1.71 ± 0.02	1.34 ± 0.09	1.76 ± 0.01	1.50 ± 0.02	1.23 ± 0.05

The errors were calculated from two independent repeats of the experiment.

Table S12. Enzymatic activity parameters of ΔN-ClpB and its pore loop mutants.

ClpB variant	V_{max} (1/min)	$K_{0.5}$ (μM)	n	Dissaggregation rate (nM/min)
WT	4.5 ± 0.5	300 ± 20	2.0 ± 0.2	3.89 ± 0.43
Y1	4.8 ± 0.1	450 ± 20	2.2 ± 0.2	2.35 ± 0.39
Y3	2.2 ± 0.1	430 ± 40	2.7 ± 0.6	1.07 ± 0.33
Y1-Y3	2.2 ± 0.1	730 ± 50	2.0 ± 0.2	0.3 ± 0.32

Parameters obtained from fits of ATPase activity of ΔN-ClpB and its pore loop mutants to the Hill equation, see the Methods section “ATPase activity”. Errors were obtained from two repeats of the experiment.